Dissecting the role of initial collision geometry for jet quenching observables in relativistic heavy ion collisions

Jiangyong Jia[1,2,*] and Rui Wei[1]

[1] *Department of Chemistry, Stony Brook University, Stony Brook, NY 11794, USA*
[2] *Physics Department, Brookhaven National Laboratory, Upton, NY 11796, USA*

(Dated: April 30, 2010)

The observation of large azimuthal anisotropy or v_2 for hadrons above $p_T > 5$ GeV/c in Au+Au collisions at $\sqrt{s_{\rm nn}} = 200$ GeV has been a longstanding challenge for jet quenching models based on perturbative QCD (pQCD). Using a simple jet absorption model, we seek to clarify the situation by exploring in detail how the calculated v_2 varies with choices of the collision geometry as well as choices of the path length dependence and thermalization time τ_0 in the energy loss formula. Besides the change of eccentricity due to distortion from gluon saturation or event-by-event fluctuation, we find that the v_2 is also sensitive to the centrality dependence of multiplicity and the relative size between the matter profile and the jet profile. We find that the v_2 calculated for the naive quadratic path length dependence of energy loss, even including eccentricity fluctuation and the gluon saturation, is not enough to describe the experimental data at high p_T ($\sim$ 6 GeV/c) in Au+Au collisions. However, it can match the full centrality dependence of v_2 data if higher order path length dependence of energy loss is allowed. We also find that the calculated v_2 is sensitive to the assumption of the early time dynamics but generally increases with τ_0, opposite to what one expects for elliptic flow. This study attests to the importance of confining the initial geometry, possibly by combining jet quenching v_2 with elliptic flow and other jet quenching observables, for proper interpretation of the experimental data.

PACS numbers: 25.75.-q

I. INTRODUCTION

After the discovery of the strongly interacting Quark Gluon Plasma (sQGP) at the Relativistic Heavy Ion Collider (RHIC) in 2005 [1], the focus of the heavy ion community is shifted towards a detailed characterization of the properties of the sQGP. One of the primary tools is jet quenching or the suppression of high transverse momentum (p_T) hadron yields as a result of in-medium radiative energy loss of high p_T jets [2–4]. Due to large momentum scale of the jets and asymptotic freedom of Quantum Chromodynamics (QCD), jet quenching is usually described by the pertubative QCD (pQCD) framework, which assumes that jets couple weakly with the medium, even though the medium itself is strongly coupled. Jet quenching models based on pQCD have been developed to describe measurements on single hadron yield [5, 6], dihadron correlation [7, 8] and γ-hadron correlation [9–12]. Initial estimates of the properties of sQGP, such as the momentum broadening per mean free path, $\hat{q} = \langle k_T^2 \rangle / \lambda$, and energy loss per unit length, dE/dl, have been obtained [13].

Despite its early successes, the pQCD description of jet quenching faces several challenges (see Ref [14]). one observable that has thus far defied the pQCD description is high p_T v_2 or azimuthal anisotropy of particles emission relative to the reaction plane (RP) in Au+Au collisions, $dN/d(\phi - \Psi_{\rm RP}) \propto (1 + 2v_2 \cos 2(\phi - \Psi_{\rm RP}))$.

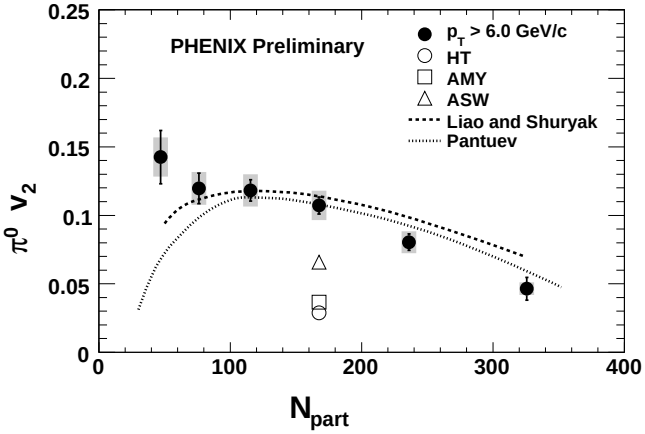

FIG. 1: Figure adapted from [18]. Data points: PHENIX π^0 v_2 at p_T >6GeV/c. Open symbols: three pQCD model calculations taken from [13]. Lines: geometric model calculations with different assumptions on path length dependence [24, 54].

Such azimuthal anisotropy ensues because jet yield is more suppressed along the long axis of the fireball (out-of-plane) than the short axis (in-plane). Thus the v_2 value is sensitive to the path length (l) dependence of energy loss, which scales, in pQCD framework, as $\Delta E \propto l$ and $\Delta E \propto l^2$ for elastic and radiative energy loss [15], respectively. Currently, most pQCD models undershoot the v_2 value by as much as factor of 2 in experimentally accessible p_T range ($p_T < 10$ GeV/c) [16, 17]. We illustrate this situation with Fig. 1 borrowed from Ref. [18], which compares three mainstream pQCD model calcula-

*Correspond to jjia@bnl.gov

tions (abbreviated as AMY, ASW, HT) [13] with recent precision PHENIX data at $p_T \sim 6$ GeV/c.

This, together with its failure in describing heavy flavor suppression [19] call into question the perturbative assumption used in the pQCD framework. It may happen that the coupling between the jet and the medium for typical RHIC jet energy of $p_T \lesssim$ 10-20GeV/c is still strong enough [20], such that path length dependence and the color charge dependence are modified from pQCD expectation. In fact, calculation based on AdS/CFT technique for strongly coupled plasma suggests that $\Delta E \propto l^3$ [21] and $\hat{q} \propto \sqrt{\alpha_{\rm SYM} N_c}$ [22], instead of $\Delta E \propto l^2$ and $\hat{q} \propto \alpha_s N_c^2$ for pQCD. This higher order path length dependence could explain the large anisotropy [23]. Liao & Shuryak [24] argue that most energy loss in sQGP is concentrated around T_c; such a non-monotonic dependence of energy loss with energy density apparently achieves better description of the data as shown by Fig. 1.

It is tempting to conclude from this discussion that the data favor a l dependence stronger than the naive $\Delta E \propto l^2$ implied by the pQCD radiative energy loss. However, as being pointed out in [17], the magnitude of the anisotropy is also very sensitive to the choice of initial collision geometry, which is poorly constrained. The collision geometry used by most jet quenching calculations is obtained from the so called Optical Glauber model [25], which assumes smooth Woods-Saxson nuclear geometry for Au ions. It ignores two important modifications: a event-by-event distortion of the shape of the overlap from random fluctuation of positions of participating nucleons [27]; and a possible overall distortion of the shape of the overlap due to gluon saturation effect (so called CGC geometry [26]). Both effects are shown to lead to 15-30% corrections in the hydrodynamic calculation of elliptic flow at low p_T [29]; they were also shown in Ref. [26, 30] to play an important role for jet quenching calculation of azimuthal anisotropy at high p_T.

Furthermore, the way that collision geometry influence the jet quenching v_2 is quite different from that for hydrodynamic description of low p_T v_2. Hydrodynamic flow is a self generating process driven by the shape or eccentricity ($\epsilon = \frac{\langle y^2\rangle - \langle x^2\rangle}{\langle y^2\rangle + \langle x^2\rangle}$) of a single matter profile, i.e. $v_2 \propto \epsilon$; whereas the v_2 from jet quenching requires both the profile for the bulk matter AND the jet production points. The two profiles may not necessarily have the same spatial distribution since various nuclear effects at initial state may induce sizable momentum (a.la Bjorken momentum fraction $2p_T/\sqrt{s}$) and position dependent modification, analogous to the generalized parton distribution for proton. Hence high p_T v_2 depends not only on the eccentricity of the fireball, but also on the matching (relative size and shape) between the jet and the matter profiles.

In this paper, we investigate the sensitivity of the jet quenching v_2 on the choices/uncertainties of the collision geometry for the bulk matter. We check explicitly the scaling and violation thereof with the bulk eccentricity. We explore, in the context of these uncertainties, whether the data allow for high order l dependence of energy loss. The prospects of constraining the initial collision geometry using v_2 and other jet quenching observables, such as single inclusive suppression $R_{\rm AA}$, inclusive away-side suppression $I_{\rm AA}$ and associated anisotropy $v_2^{I_{\rm AA}}$, are discussed.

II. MODEL IMPLEMENTATION

We generate the Glauber geometry using an improved version of the publicly available PHOBOS code [31]. Each Au ion is populated randomly with nucleons with a hard-core of 0.3 fm in radii, according to the Woods-Saxson distribution with a radius of 6.38 fm and diffuseness of 0.535 fm. A nucleon-nucleon collision is considered to happen when their distance in the xy-plane fall within $\sqrt{\sigma_{\rm nn}^{\rm inel}/\pi} = 1.16$ fm (hard-sphere assumption), corresponding a n-n cross-section of $\sigma_{\rm nn}^{\rm inel}$=42 mb. Subsequently the number density of nucleons participating in the collision ($\rho_{\rm part}(x,y,b)$) and the number density of binary collisions ($\rho_{\rm coll}(x,y,b)$) can be determined in the xy-plane as function of impact parameter b. Here x direction is always chosen to be along the line connecting the centers of the two ions. Denoting T_A as the thickness function for Au ion, they can be approximated with the following expression when nucleon size is ignored.

$$\begin{aligned}
\rho_{\rm part}(x,y,b) &\approx T_A\left(x+\frac{b}{2},y\right)\left[1-P\left(x+\frac{b}{2},y\right)\right] \\
&+ T_A\left(x-\frac{b}{2},y\right)\left[1-P\left(x+\frac{b}{2},y\right)\right], \\
\rho_{\rm coll}(x,y,b) &\approx \sigma_{\rm nn}^{\rm inel} T_A\left(x+\frac{b}{2},y\right) T_A\left(x-\frac{b}{2},y\right), \quad (1)
\end{aligned}$$

where $P(x,y) = \left(1-\frac{\sigma_{\rm nn}^{\rm inel} T_A(x,y)}{A}\right)^A$ and $A = 197$ is the number of nucleons in Au ion.

We generate the CGC geometry using the MC-KLN model by Dresher & Nara [26, 28], which is based on the well known KLN (Kharzeev-Levin-Nardi) k_T factorization approach [32]. In a nutshell, MC-KLN model calculate the CGC geometry event by event by modifying the output from a Monte-Carlo Glauber model. Specifically, the transverse gluon density profile, $dn/dy(x,y,b)$, is calculated through the k_T factorization formula, with the saturation scale Q_s^2 of each Au ion set to be proportional to its thickness function T_A or T_B. To insure internal consistency, the MC-KLN code is adapted to the same Glauber algorithms as PHOBOS code(same hard-core nucleons and identical Woods-Saxson parameters). The obtained gluon density scales approximately [26] as $\min\{T_A, T_B\}$ in the x direction and $1/2(T_A+T_B)$ in the y direction, which leads to a 20-30% increase of the eccentricity relative to the Glauber geometry (see left panels of Fig. 5). When implemented in hydrodynamic model calculations [29], a similar amount of increase is seen for the predicted elliptic flow signal.

We account for initial geometry fluctuation in Glauber geometry by re-centering and rotating all participants, such that the "participant plane" (PP), defined as the minor axis direction of all participants, aligns with the lab frame. We then sum all events together to give the overall participant density profile. The same amount of shift and rotation is then applied for all binary collisions to get the overall density profile for jet production points. We repeat the same procedure to the gluon density profile for CGC geometry. Important variables include the orientation of the participant plane ($\Psi_{\rm part}$) for either participants or gluon density, eccentricity with respect to the reaction plane ($\epsilon_{\rm RP}$), eccentricity with respect to the participant plane ($\epsilon_{\rm part}$) and average root mean square (RMS) size of the ellipsoid (σ_r). They are calculated for each event as

$$\begin{aligned}
\tan(2\Psi_{\rm part}) &= \frac{\sigma_y^2-\sigma_x^2}{2\sigma_{xy}^2} \\
\epsilon_{\rm RP} &= \frac{\sigma_y^2-\sigma_x^2}{\sigma_y^2+\sigma_x^2} \\
\epsilon_{\rm part} &= \frac{\sqrt{(\sigma_y^2-\sigma_x^2)^2+4\sigma_{xy}^2}}{\sigma_y^2+\sigma_x^2} = \frac{\sigma_y'^2-\sigma_x'^2}{\sigma_y'^2+\sigma_x'^2} \\
\sigma_r^2 &= \sigma_y^2+\sigma_x^2 = \sigma_y'^2+\sigma_x'^2
\end{aligned} \tag{2}$$

where σ_x^2, σ_y^2 and σ_{xy} are the event-by-event (co)variances of participant density profile for Glauber geometry or gluon density profile for CGC geometry, respectively, and $\sigma_x'^2$ and $\sigma_y'^2$ are variances defined in the rotated frame. We emphasize that the participant plane angle, $\Psi_{\rm part}$, should be the natural frame for both hydrodynamic flow and jet quenching. However, it is tilted by different amount in the case of the CGC geometry from the Glauber geometry.

In this work, the magnitude of the jet quenching v_2 depends on the following four control factors:

1. **Energy loss formula**, including the path length dependence, thermalization time etc.
2. **Eccentricity**, including event-by-event fluctuation and the shape of collision geometry (e.g. CGC vs Glauber).
3. **Centrality dependence of the total multiplicity**. Since the jet quenching strength is fixed in most central collision, if matter density falls faster towards peripheral collisions, we expect less suppression and smaller v_2 in peripheral collisions.
4. **The size of the matter profile relative to the jet profile**. If the transverse size of the matter profile is smaller than that for the jet profile, more surviving jets should originate from the corona region, leading to a smaller v_2.

Clearly, the collision geometry (item 2-4) plays essential roles for proper understanding of the energy loss mechanism (item 1). In contrast to hydrodynamic description of low p_T v_2, which depends only on the eccentricity of the ellipsoid, jet quenching description of high p_T v_2 is sensitive to two more aspects of the collision geometry (item 3-4). The primary goal of this work is to understand how the jet quenching v_2 depends on the underlying choices of eccentricity, centrality dependence of multiplicity and matching between the matter and jet profile.

We base the study on following four matter profiles (three versions of Glauber geometry and one CGC geometry)

$$\begin{aligned}
\rho_0(x,y,b) &= \rho_{\rm part}(x,y,b) \\
\rho_1(x,y,b) &= \rho_{\rm coll}(x,y,b) \\
\rho_2(x,y,b) &= \frac{1-\delta}{2}\rho_{\rm part}(x,y,b)+\delta\rho_{\rm coll}(x,y,b) \\
\rho_3(x,y,b) &= \rho_{\rm CGC}(x,y,b) = dn/dy(x,y,b)
\end{aligned}$$

with the corresponding integral form

$$\begin{aligned}
\int dxdy\ \ \rho_0(x,y,b) &= N_{\rm part}(b) \\
\int dxdy\ \ \rho_1(x,y,b) &= N_{\rm coll}(b) \\
\int dxdy\ \ \rho_2(x,y,b) &= \frac{1-\delta}{2}N_{\rm part}(b)+\delta N_{\rm coll}(b) \\
&\approx dN/dy(b) \\
\int dxdy\ \ \rho_3(x,y,b) &= dN/dy(b)
\end{aligned} \tag{3}$$

Where $\rho_{\rm part}$ and $\rho_{\rm coll}$ are transverse participant density and collision density from Glauber model, respectively; ρ_2 is the two component Glauber model from [33] with $\delta = 0.14$ [29] and $\rho_3 = \rho_{\rm CGC}$ is the transverse gluon density from MC-KLN. Both ρ_2 and ρ_3 has been adjusted [29] such that their total integral match the centrality dependence of the charged hadron multiplicity, $dN/dy(b)$, at RHIC [34]. For the first two profiles, ρ_0 and ρ_1, we can enforce the same centrality dependence as $dN/dy(b)$ by applying a centrality dependent scale factor:

$$\begin{aligned}
\rho_0^{\rm Mul}(x,y,b) &= \frac{dN/dy(b)}{N_{\rm part}(b)}\rho_{\rm part}(x,y,b) \\
\rho_1^{\rm Mul}(x,y,b) &= \frac{dN/dy(b)}{N_{\rm coll}(b)}\rho_{\rm coll}(x,y,b) \\
\int dxdy\ \ \rho_0^{\rm Mul}(x,y,b) &= dN/dy(b) \\
\int dxdy\ \ \rho_1^{\rm Mul}(x,y,b) &= dN/dy(b)
\end{aligned} \tag{4}$$

These scale factors essentially accounts for the different centrality dependence trends between $N_{\rm part}$ and $N_{\rm coll}$ rel-

ative to dN/dy. Fig. 2 shows the rate of change of dN/dy and $N_{\rm coll}$ relative to $N_{\rm part}$ normalized to unity for most central points. Clearly the $N_{\rm coll}$ has the fastest change vs. centrality, followed by dN/dy, and $N_{\rm part}$ has the slowest change vs. centrality. Nevertheless, the resulting profiles, $\rho_0^{\rm Mul}$ and $\rho_1^{\rm Mul}$, still maintain their original shape and size. They are used to study the sensitivity of v_2 to the centrality dependence of the multiplicity.

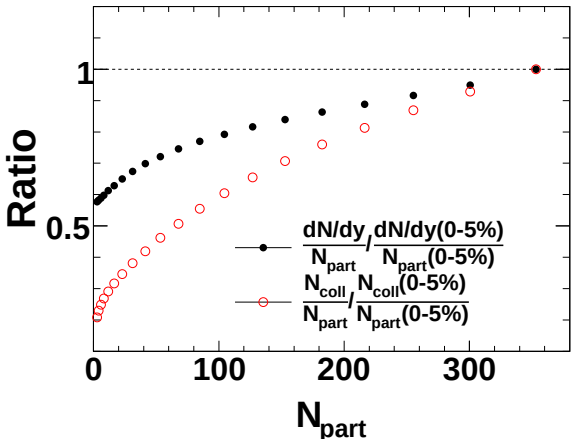

FIG. 2: (Color online) The centrality dependence of $dN/dy/N_{\rm part}$ (filled) and $N_{\rm coll}/N_{\rm part}$ (open) normalized by their values in most central 0-5% bin. This plot illustrates different rates of change as a function of centrality, between $N_{\rm part}$, $N_{\rm coll}$ and dN/dy.

Besides the two profiles obtained by matching to dN/dy, we are also interested in several other variants of $\rho_0-\rho_3$, obtained either by rotation of their respective participant planes [1],

$$\rho_n^{\rm Rot}(x,y) = \rho_n(x\cos\Psi_{\rm part} - y\sin\Psi_{\rm part}, \\ x\sin\Psi_{\rm part} + y\cos\Psi_{\rm part}),$$

or by re-adjusting the overall size by a constant scale factor a to match to that of ρ_0 (see discussions in Section III B and III C)

$$\rho_n^{\rm Resize}(x,y) = \rho_n(ax,ay),$$

or by a combination of matching multiplicity, rotation or readjusting size. In the case that a profile is obtained via several operations, we use appropriate superscript to indicate that. For example, $\rho_0^{\rm Rot,Mul}$ indicates the matter profile obtained by rotating the event-by-event participant profile according to the participant plane angle, followed by matching its total integral to dN/dy for each centrality bin. Note the order of these operations has no significance since they factorize.

We implement jet quenching using the simple jet absorption model of Ref. [17]. It provides a transparent way to investigate the sensitivity of jet quenching observables to choices of the collision geometry. In this model, back-to-back jet pairs are generated according to the binary collision density profile in xy-plane with uniform orientation. These jets are then propagated through the medium whose density is given by matter profile $\rho(x,y)$, with a survival probability $e^{-\kappa I}$. In the default setup, matter integral I is calculated as

$$I = \int_0^\infty dl \frac{l}{l+l_0}\rho(\vec{\mathbf{r}} + (l+l_0)\,\hat{\mathbf{v}}) \approx \int_0^\infty dl\ \rho(\vec{\mathbf{r}} + l\hat{\mathbf{v}}) \quad (5)$$

for jet generated at $\vec{\mathbf{r}} = (x,y)$ and propagated along direction $\hat{\mathbf{v}}$. This corresponds to a quadratic dependence of absorption ($\propto ldl$) in a longitudinal expanding or 1+1D medium ($\propto 1/(l_0+l)$) with a thermalization time of $l_0 = c\tau_0$. It is fixed to 0 by default but we explore non-zero value of l_0 in Section III E. The absorption coefficient κ (which controls the jet quenching strength) is chosen to reproduce $R_{\rm AA} = \langle e^{-\kappa I}\rangle \sim 0.18$ for 0-5% π^0 data [37]. We explore path length dependence by extending Eq. 5 to four different functional forms,

$$I_m = \int_0^\infty dl\ l^{m-1}\ \rho(\vec{\mathbf{r}} + l\hat{\mathbf{v}}), \qquad m = 1,2,3,4. \quad (6)$$

$m=1$ and $m=2$ correspond to l dependence for elastic, radiative, and AdS/CFT energy loss in 1+1D medium, respectively.

A typical calculation starts by choosing one of the four matter profiles (Glauber geometry $\rho_0-\rho_2$ or CGC geometry ρ_3) and applying appropriate modifications (specifying Rot, Mul, and/or Resize). We specify the jet absorption scheme by varying thermalization time l_0 or the order of path length dependence m. We then fix the κ value by matching $R_{\rm AA} \sim 0.18$ in most central collision. On the other hand, the jet production profile is always given by $\rho_{\rm coll}$. We stress that κ is the only free parameter, and has similar role as the $\hat{q}$, and it is tuned independently for each one of these running modes. Once κ is known, we can predict the centrality dependence of the single hadron suppression ($R_{\rm AA}$), jet quenching v_2 which can be expressed as $v_2 = \langle e^{-\kappa I}\cos 2\,(\phi - \Psi_{\rm part})\rangle$, and away-side per-trigger yield suppression ($I_{\rm AA}$).

III. RESULTS

A. Glauber geometry based on participant profile

As mentioned previously, this work investigates three versions of Glauber geometry, participant profile ρ_0, collisional profile ρ_1 and two component profile ρ_2 and their variants. ρ_0 is our default Glauber geometry and is the topic of this section, we shall discuss ρ_1 and ρ_2 in Sec-

[1] Note that the participant plane angle $\Psi_{\rm part}$ is defined separately for ρ_0-ρ_3. For ρ_1, it is determined by the minor axis of all binary collisions, while that for ρ_2 is determined by both participants and binary collision with appropriate weights given in Eq. 3.

tion III C.

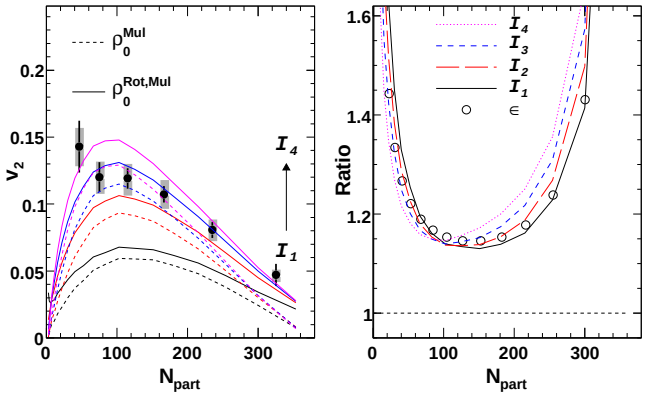

FIG. 3: (Color online) Left: v_2 calculated with $\rho_0^{\rm Mul}$ (participant density profile scaled to match dN/dy) with (solid lines) and without (dashed lines) rotation to the participant plane compared with data at 6 GeV/c (solid circles) for $I_1 - I_4$ (from bottom up); Right: Corresponding ratios between with to without rotation for $I_1 - I_4$ (lines) and for the eccentricity (open circles). I_0 is omitted for clarify.

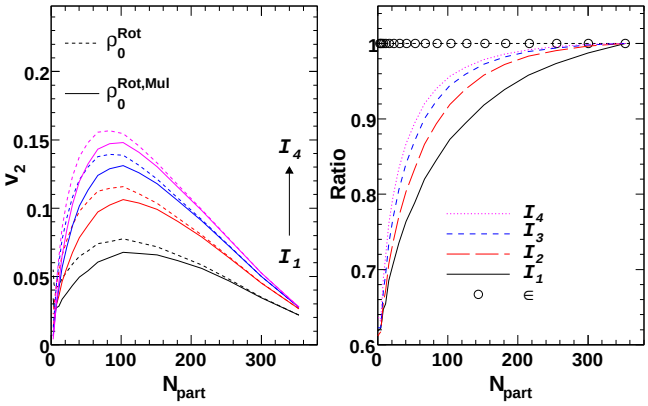

FIG. 4: (Color online) Left: v_2 calculated with $\rho_0^{\rm Rot}$ (participant density profile rotated to participant plane) with (solid lines) and without (dashed lines) scaling to match dN/dy for $I_1 - I_4$ (from bottom up); Right: Corresponding ratios between with to without scaling to dN/dy for $I_1 - I_4$ (lines) and for the eccentricity (open circles). Note that the eccentricities are identical for the two cases.

Fig. 3 shows the v_2 calculated for Glauber geometry $\rho_0^{\rm Mul}$, i.e. participant profile scaled to match the experimental multiplicity. Results are presented in left panel for four different path length dependence ($I_1 - I_4$ from bottom to top) with (solid lines) and without (dashed lines) taking into account the fluctuation of PP angle. They are compared with the PHENIX π^0 v_2 data integrated above 6 GeV/c from Fig.1. The right panels show the ratios of calculated v_2 for $I_1 - I_4$ (solid lines) and the ratio of the eccentricity (open circles) between with and without including the fluctuations.

We see that increasing m (the order of l dependence) significantly increases the v_2 for mid-central collisions, but they all systematically under-shoot the data towards central collisions. In fact, the calculated v_2 for central collision is insensitive to the functional form of path length dependence, due to the almost isotropic shape of the overlap. This situation is dramatically improved when the fluctuation in the PP angle is included. The relative increase in v_2 is about 15% for mid-centrality, and is significantly larger for central and peripheral collisions. This is consistent with previous studies of low p_T v_2 or elliptic flow, which shows that PP fluctuation needs to be included in Cu+Cu and central Au+Au collisions in order for hydrodynamic model prediction to work [27, 38]. It is interesting to see the fractional increase of v_2 for I_1 is similar to the fractional increase in eccentricity (i.e $\epsilon_{\rm part}/\epsilon_{\rm RP}$ in the right panel). However, the fractional increase at $N_{\rm part} > 50$ is successively larger from I_1 to I_4. This is because larger m places more weight to large l region, thus is more sensitive to changes in shape.

The high p_T azimuthal anisotropy, being the result of jet quenching, depends not only on the shape, but also on the average density or total multiplicity of the matter profile. To illustrate this point, Fig. 4 shows the v_2 calculated for matter density $\rho_0^{\rm Rot}$ and $\rho_0^{\rm Rot,Mul}$. They have identical shape and size for each centrality selection, but the integral of $\rho_0^{\rm Rot,Mul}$ drops more rapidly to lower $N_{\rm part}$. Because jet absorption strength κ is tuned to reproduce a common suppression level in central collision, the profile whose average density varies more rapidly with centrality is expected to show less suppression and less v_2 in peripheral collisions. Indeed, the calculated v_2 for $\rho_0^{\rm Rot,Mul}$ is smaller than that for $\rho_0^{\rm Rot}$ due to a faster fall off towards peripheral bin.

Fig. 4 also shows a weakening of the sensitivity for larger m. This is because the weighting from large l region is reduced in peripheral collisions due to a smaller geometrical size. That reduction is stronger for larger m, which leads to smaller sensitivity for large m.

One may argue that since $dN/dy(b)$ is constrained by experimental data, there should be no uncertainty associated with the modeling of centrality dependence. However, the matter profiles that were tuned to Au+Au 200 GeV data typically shows $\sim 10\%$ deviation from Cu+Cu or Au+Au at different collision energies [39, 40]. Furthermore, many current pQCD model calculations use profiles that do not match the dN/dy data. For example, various 1+1D energy loss models assumes energy loss or $\hat{q}$ to be proportional to either $\rho_{\rm part}$ [8, 20, 41] or $\rho_{\rm coll}$ [42]; Recent more sophisticated calculations [12, 13, 43] based on 3D+1 hydrodynamics model of Nonaka & Bass [44], assume the energy loss or $\hat{q} \propto e^{3/4}$ with $e \propto 0.6\rho_{\rm coll} + 0.4\rho_{\rm part}$ [44], which is also different from dN/dy. So it seems reasonable to use the difference of the v_2 in right panel of Fig. 4 as one of the uncertainties in theoretical implementation of initial geometry.

Fig. 3 and Fig. 4 represent the general style of the presentation of the v_2 calculation in this paper: the left

panel always shows the v_2 values for $I_1 - I_4$ compare between two matter profiles with (solid lines) and without (dashed lines) a particular geometrical effect; the right panel always shows the ratios between the two (solid line divided by dashed line). In most cases, the ratio of their eccentricities is shown as open circles on the right panel to compare with v_2 ratios. Finally, we stress that the jet production profiles are always sampled from $\rho_{\rm coll}$ throughout this study, so whatever difference in the calculated v_2 can be attributed to the differences between the two matter profiles.

B. CGC geometry

As outlined in the introduction, MC-KLN model is built on the standard Monte-Carlo Glauber model. So CGC matter profile ρ_3 contains both the overall modification of shape due to gluon saturation, and the event-by-event fluctuation stemming from participant fluctuation at Glauber level. In addition, we can safely use the same binary collision profile for the jet production, given that the saturation effects are not expected to modify hard processes with momentum transfer well above the saturation scale, $Q^2 \gg Q_s^2$.

Another important feature of the CGC geometry via MC-KLN model is that despite having a larger eccentricity, its overall size is about 4-8% smaller than the participant profile. One can see it quantitatively in Fig. 5, which compare the eccentricity and overall RMS width (σ_r) between ρ_3 and ρ_0. This narrowing of CGC geometry was pointed out before by the authors of MC-KLN model (see the preprint version of [26]), and can be seen more clearly by plotting the 1D projections of medium profiles along the x (in-plane) and y (out-of-plane) directions (Fig. 6). The projections show that CGC profile is narrower than Glauber profile in both x and y direction, however the difference is larger in the x direction, leading to a larger eccentricity.

Fig. 7 compare the v_2 calculated for CGC geometry (ρ_3) and Glauber geometry (ρ_0) in their respective rotated frames. The CGC geometry does lead to a larger v_2, however, the amount of increase is only half of the increase in eccentricity. To check whether the breaking of the eccentricity scaling can be attributed to the 4-8% mismatch between the two profiles, we re-scale the RMS size of the CGC geometry to match that for the Glauber geometry for each centrality while preserving its original shape. Fig. 8 shows the same comparison after the scaling is applied. The ratios of the calculated v_2 now match well with the ratio of the eccentricities.

These comparison plots clearly show that both eccentricity and the size contribute to the difference of the v_2 between CGC and Glauber geometry: While the eccentricity of the CGC geometry increase by about 10-30% relative to Glauber geometry, its transverse size shrinks. The latter change increases the fractional contribution of surface jets, which have smaller v_2. In contrast, there is

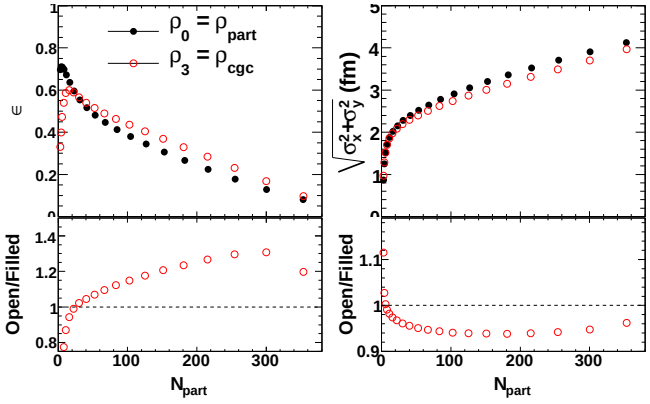

FIG. 5: (Color online) Left: Eccentricities for Glauber geometry calculated from participant density profile ρ_0 (solid circles) and for CGC geometry ρ_3 (open circles) in the top panel and the corresponding ratio in the bottom panel. Right: Same as right panels except they are for the RMS size $\sigma_r = \sqrt{\sigma_x^2 + \sigma_y^2}$.

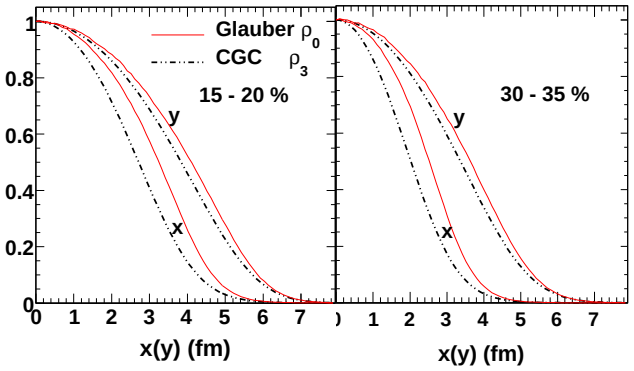

FIG. 6: (Color online) The Glauber geometry (ρ_0) and CGC geometry (ρ_3) projected on to x and y axis for 15-20% and 30-35% centrality bins.

no such bias for hydrodynamic calculation of low p_T v_2, which depends on the shape, not the size, of the matter profile.

C. Glauber geometry based on collision profile and two component profile

The above discussion alludes to an interesting possibility: For given energy loss formula and jet production profile, as long as the matter profile is adjusted to a common reference σ_r and dN/dy, the v_2 depends only on the eccentricity of the matter profile. Here we further test this ansatz by using a matter profile ρ_1 that is very different from ρ_0. Comparing to the ρ_0, ρ_1 has much larger eccentricity (left panels of Fig. 9) which should increase the calculated v_2. On the one hand, it has substantially stronger centrality dependence (Fig. 2) and 10-15% smaller σ_r (right panels of Fig. 9), both are expected to significantly decrease the calculated v_2.

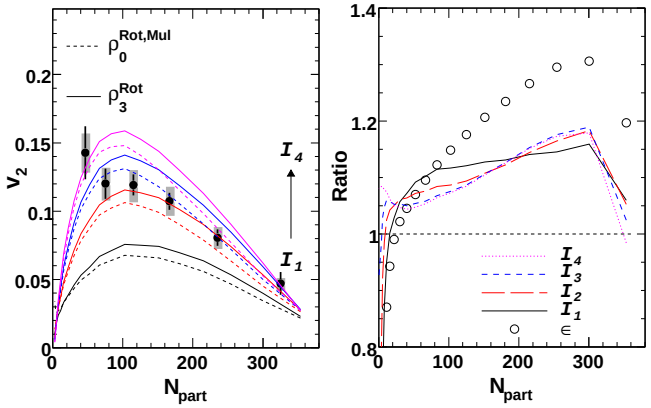

FIG. 7: (Color online) Left: v_2 calculated for Glauber geometry (ρ_0^{Rot}) and CGC geometry (ρ_3^{Rot}) in their respective rotated frames for $I_1 - I_4$ (from bottom up). Right: Corresponding ratios for $I_1 - I_4$ (lines) and for the eccentricity (open circles). Note that the CGC geometry has larger eccentricity.

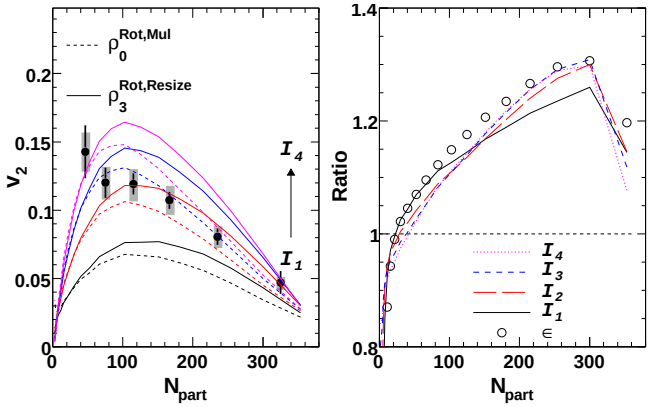

FIG. 8: (Color online) Same as Fig. 7, except that the RMS size of CGC geometry has been stretched to match Glauber geometry ρ_0 (according to ratio shown in bottom right panel of Fig. 5)

Fig. 10 compares the v_2 calculated for ρ_1 and ρ_0 in their respective rotated frames. The calculated v_2 falls well below the experimental v_2 data in central collisions, which suggests that the Glauber geometry based solely on collision density profile with eccentricity fluctuation is ruled out. The decrease of the v_2 is largely due to the stronger centrality dependence and smaller size of ρ_1, and can be seen more quantitatively in the right panel, which appears as a large suppression of the v_2 ratios from the expected eccentricity ratio.

To dissect the impacts of these factors more clearly, we calculate the v_2 of ρ_1 in three different ways before making the ratio with the v_2 of $\rho_0^{\mathrm{Rot,Mul}}$: 1) original multiplicity and size, ρ_1^{Rot} 2) multiplicity is adjusted to match dN/dy or $\rho_0^{\mathrm{Rot,Mul}}$, $\rho_1^{\mathrm{Rot,Mul}}$ 3) both multiplicity and size adjusted to match $\rho_0^{\mathrm{Rot,Mul}}$, $\rho_1^{\mathrm{Rot,Mul,Resize}}$. The results are shown in Fig. 11 for $m = 1$ (top-left panel), $m = 2$ (top-right panel), $m = 3$ (bottom-left panel), and $m = 4$

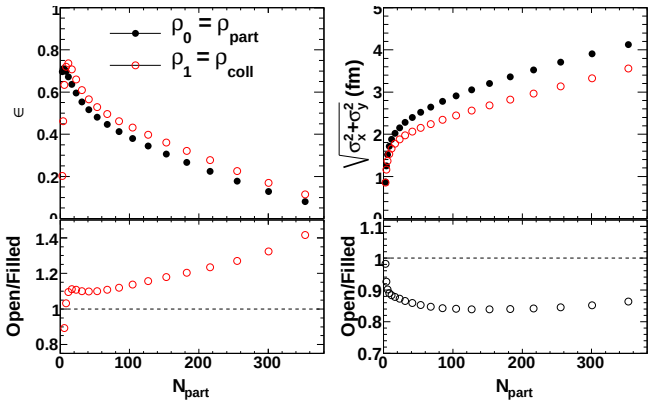

FIG. 9: (Color online) Left: Eccentricities for Glauber geometry calculated from participant density profile ρ_0 (solid circles) and from collision density profile ρ_1 (open circles) in the top panel and the corresponding ratio in the bottom panel. Right: Same as right panels except they are for the RMS size $\sigma_r = \sqrt{\sigma_x^2 + \sigma_y^2}$.

(bottom-right panel). We see that matching the multiplicity dependence mostly increases v_2 at $N_{\mathrm{part}} < 200$ where the dN/dy per participant is changing the fastest, but has very little influence at $N_{\mathrm{part}} > 200$. However, after the RMS size of the matter profile is readjusted to match that of participant profile, the calculated v_2 ratios follow the ratio of the eccentricities nicely (except in central and peripheral bins for $m > 1$). We clearly see a large sensitivity of v_2 on σ_r: the large ($\sim 50\%$) suppression of v_2 in central collisions, i.e. difference between dashed line and solid circles, is mostly due to a $\sim 15\%$ narrowing of σ_r (Fig. 9).

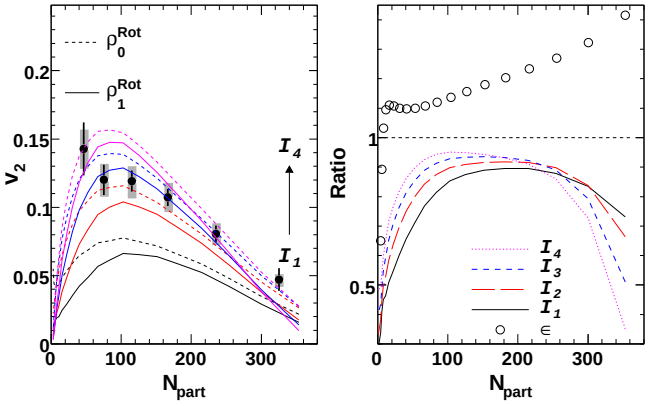

FIG. 10: (Color online) Left: v_2 calculated for two Glauber geometries, ρ_0^{Rot} and ρ_1^{Rot}, in their respective rotated frames for $I_1 - I_4$ (from bottom up). Right: Corresponding ratios for $I_1 - I_4$ (lines) and for the eccentricity (open circles). Note that ρ_1^{Rot} (collision density profile) has larger eccentricity.

It is now straightforward to apply what we learned from Fig. 11 to study the v_2 for the two component matter profile, ρ_2. ρ_2 is built as a linear combination of participant density profile (ρ_1) and collision density pro-

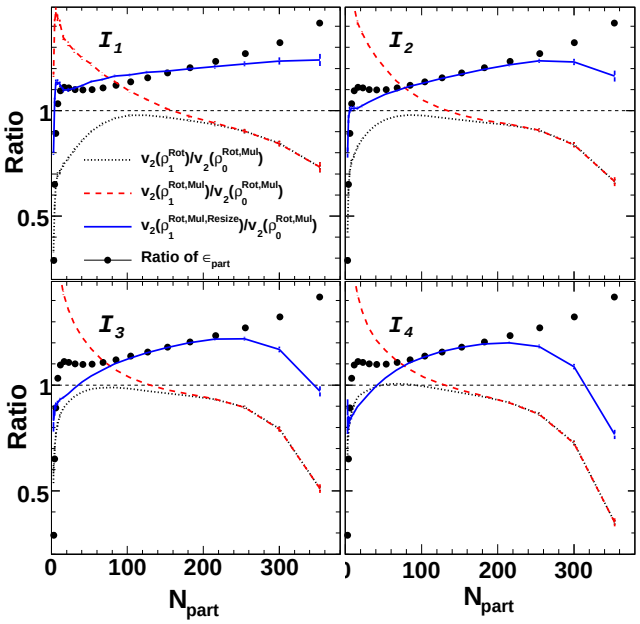

FIG. 11: (Color online) Ratios of calculated v_2 between $\rho_0^{\rm Rot,Mul}$ and three cases of $\rho_1^{\rm Rot}$: original multiplicity and size (dotted lines), multiplicity is adjusted to match dN/dy or $\rho_0^{\rm Rot,Mul}$ (dashed lines), both multiplicity and size adjusted to match $\rho_0^{\rm Rot,Mul}$ (solid lines). They are presented separately for I_1 (top left panel), I_2(top right panel), I_3(bottom left panel) and I_4(bottom right panel).

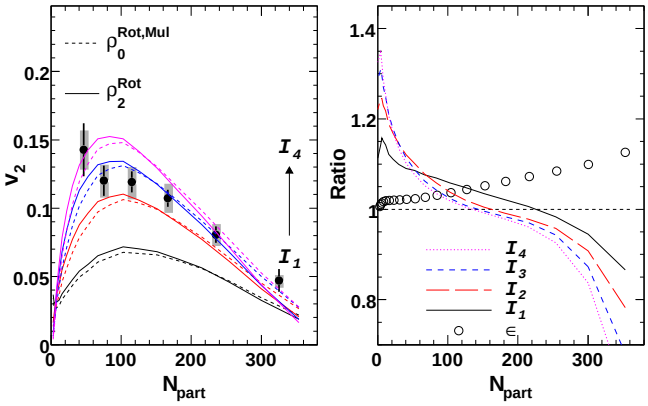

FIG. 12: (Color online) Left: v_2 calculated for two Glauber geometries, $\rho_0^{\rm Rot}$ and $\rho_2^{\rm Rot}$, in their respective rotated frames for $I_1 - I_4$ (from bottom up). Right: Corresponding ratios for $I_1 - I_4$ (lines) and for the eccentricity (open circles). Note that $\rho_2^{\rm Rot}$ (two component model density profile) has larger eccentricity.

file (ρ_0). It is a quite popular initial geometry used in many hydrodynamic model calculations [29, 35, 36]. It has the correct the multiplicity, but a smaller geometrical size relative to ρ_0 due to a centrality dependent contribution from binary collision density profile. We naturally expect the corresponding eccentricity and v_2 should sit in between that for ρ_0 and ρ_1. This is indeed the case as shown by Fig. 12. The ratio of the calculated v_2 between ρ_2 and ρ_0 has similar shape as the middle curve in Fig. 11, albeit the rate of change is reduced. The v_2 ratios decrease with $N_{\rm part}$, while the ratio of eccentricity increases slightly with $N_{\rm part}$. They cross each other at around $N_{\rm part} \sim 100$. In most central collisions the v_2 from two component model is suppressed by about 10%, even though the eccentricity value shows $\sim 10\%$ increase. Consequently, it under-predicts the data in central collisions (see left panel).

As a final note, we point out the mixing fraction, $\delta = 0.14$, between $N_{\rm part}$ and $N_{\rm coll}$ is chosen to match the dN/dy. However, it is not clear that this parametrization necessarily reflects the true shape and size of the matter profile (see for example [45]). This concern is especially true in viewing its poor agreement with the central data for $I_1 - I_4$ even after including the eccentricity fluctuation. Such poor agreement is clearly due to the narrow profile of the collision component in the two component profile. Nevertheless, it seems that by combining the hydrodynamic description of the low p_T v_2 and the jet quenching description of the high p_T v_2, one can gain insight not only on the eccentricity or shape, but also the size of the matter profile.

D. Fluctuations beyond rotation to the participant plane

The study of fluctuation so far only includes the fluctuation of PP angle of the initial geometry. In principle, we should also consider local density fluctuations which affect variance along the long and short axis of the ellipsoid without changing the orientation of the PP. In other words, both the size σ_r and participant eccentricity $\epsilon_{\rm part}$, which are invariant under rotation, can still fluctuate event to event for fixed impact parameter. These fluctuations are large compared to their mean values, as shown by Fig. 13.

Estimation of the influence of these additional fluctuations requires event-by-event calculation of the jet absorption, where the nucleons can not be treated as point-like object. We assume the nucleon has a gaussian profile in transverse plane with a width of r_0 in x and y direction, corresponding to a nucleon-nucleon overlap function

$$t(x,y) = \frac{1}{2\pi r_0^2} e^{-\frac{x^2+y^2}{2r_0^2}}. \qquad (7)$$

and a binary collision profile

$$\rho_{\rm coll}(x,y,b) = \int dx'dy' \quad T_A(x-\frac{b}{2},y) \times \qquad (8)$$
$$T_A(x+\frac{b}{2}+x', y+y')t(x',y')$$

The event-by-event participant profile is obtained by summing over the nucleon profile for all participants.

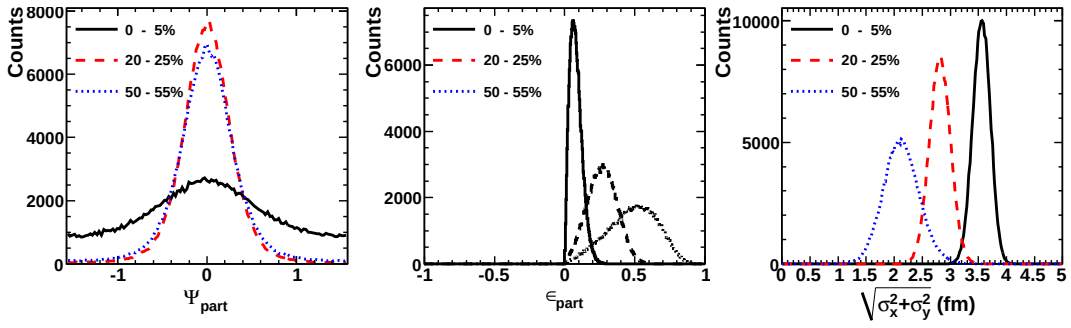

FIG. 13: (Color online) Distributions of participant plane angle (left panel), participant eccentricity (middle panel) and RMS size (right panel) for ρ_0 in three centrality selections (0-5%, 20-25% and 50-55%).

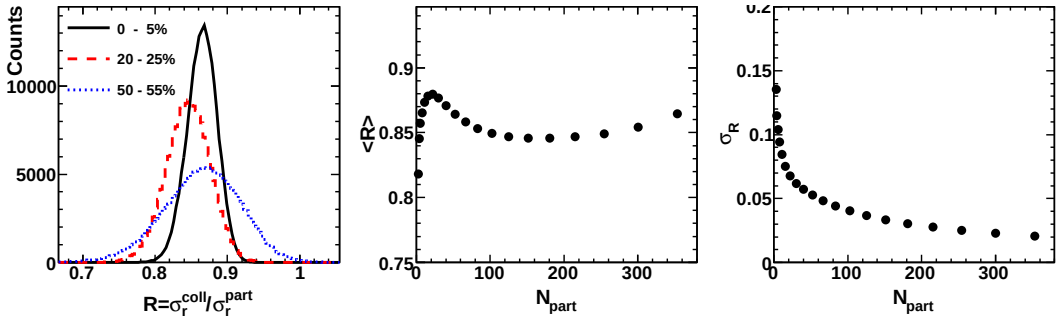

FIG. 14: (Color online) Left: Distributions of event-by-event ratio of RMS width of collision density profile to participant density profile, $R = \sigma_r^{\rm coll}/\sigma_r^{\rm part}$. Middle: centrality dependence of the mean value for R, $\langle R\rangle$. Right: centrality dependence of the RMS width for R, σ_R.

For each event, we generate 4 di-jets pairs by sampling its collision profile (Eq. 8), then calculate their absorption in corresponding participant density profile. A total of 3 million Glauber events are used. To check the stability of our result against the finite size assumption of the nucleons, we varied the r_0 from $0.2-0.4$fm, and we also assume the nucleon to be disk of constant density with a radius of $\sqrt{\sigma_{\rm nn}^{\rm inel}/\pi}/2 = 0.58$fm. It turns out the final results are not sensitive to details of the nucleon overlap function; except for very peripheral collisions ($N_{\rm part} < 20$) when nucleon size become comparable to the size of the ellipsoid. The deviation is even smaller, when average collision geometry is used. More detailed discussion on this can be found in Appendix B.

Fig. 15 shows the influences of these additional fluctuations on jet quenching v_2. Again, the jet absorption strength is tuned independently to match the central $R_{\rm AA}$ data. The main effect of these additional fluctuations is a small increase of the v_2 in central collisions and a small decrease in peripheral collisions. The change is less than 10% for $N_{\rm part} > 100$.

We can understand this 10% centrality dependence change of the jet quenching v_2 based on what was learned from previous discussion as following. First, we notice that the eccentricity averaged over many events is not the same as the eccentricity of the matter profile averaged

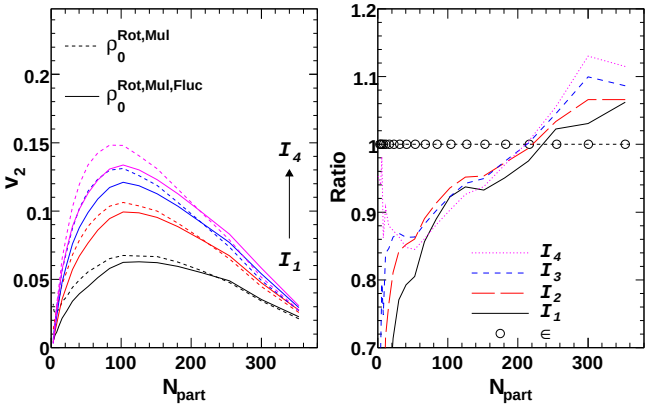

FIG. 15: (Color online) Left: v_2 for participant density profile (but in rotated frame and scaled to dN/dy), calculated either on averaged profile ($\rho_0^{\rm Rot,Mul}$) or event-by-event with additional fluctuations ($\rho_0^{\rm Rot,Mul,Fluc}$). Right: Corresponding ratios for $I_1 - I_4$ (lines) and for the eccentricity (open circles). Note that the two cases have the same eccentricities.

over many events, i.e. $\left\langle \frac{\sigma_y'^2-\sigma_x'^2}{\sigma_y'^2+\sigma_x'^2}\right\rangle \neq \frac{\langle\sigma_y'^2\rangle-\langle\sigma_x'^2\rangle}{\langle\sigma_y'^2\rangle+\langle\sigma_x'^2\rangle}$. However, Fig 26 in Appendix B shows that the difference is only about 2% and independent of $N_{\rm part}$, and can not explain the difference of the v_2 in Fig. 15. Thus it must be related to the event-by-event fluctuation of the σ_r. What

really matters is the relative size between the jet profile and matter profile, $R = \sigma_r^{\rm coll}/\sigma_r^{\rm part}$. Smaller R implies more jets are produced in the interior of the matter profile, thus suffer more energy loss and have large v_2; larger R implies more jets are produced in the corona region of the matter profile, thus suffer less energy loss and have smaller v_2.

Fig. 14 shows the distribution of R for several centralities, as well as its mean value $\langle R\rangle$ and standard deviation σ_R as a function of centrality. $\langle R\rangle$ is almost constant as function of $N_{\rm part}$ at round ~ 0.85. However the width of the distribution σ_R is a strong function of centrality, it increases from about 2% in most central collisions to more than 5% at $N_{\rm part} \sim 50$ and the distribution becomes asymmetric towards peripheral bins. It is true that the initial jet production rate does not depend on the fluctuation of R. However, the survival probability does, i.e. more jets escape the medium when R fluctuate to large value while less jets escape when R fluctuate to small value. Thus this R dependent survival probability amplifies the upward fluctuation of R, leading to a smaller v_2. The suppression of the v_2 is greater in peripheral collisions due to broader R distribution. This explained the falling of the ratio towards peripheral collisions in Fig. 15.

Before closing this section, we stress that the effect of fluctuation on v_2 can be largely attributed to the fluctuation of the PP angle. The residual effects, arising mainly from event-by-event fluctuation of the relative size between matter profile and jet production profile, is less than 10% for $N_{\rm part} > 100$. Thus it seems reasonable to use an averaged matter profile and binary collision profile for jet quenching calculation, supplemented with a small centrality dependent correction. This is of practical importance, since event-by-event jet quenching calculation is either not possible or computationally prohibitive for many current pQCD models. However, the lumpiness for event-by-event geometry implies large fluctuation of scatter centers along the jet trajectory, which may influence the Landau-Pomeranchuk-Migdal (LPM) [46] coherent effect; there is no such problem when the event average density profile is used (see Fig. 27, compare the first three panels with the bottom-right panel). However, investigation of such effects is beyond the scope of this study.

E. Dependence on the thermalization time

One of the main uncertainties in hydrodynamic description of the elliptic flow arises from modeling of the thermalization time τ_0, i.e. the time at which system reach local equilibrium and hydrodynamic expansion is turned on. This time also explicitly enters the energy loss calculation. The value of τ_0 is not known due to lack of constraints on the initial geometry and early time dynamics. Early estimation based on ideal hydrodynamics and Glauber geometry [47] shows that the RHIC v_2 data require $\tau_0 < 0.6$ fm/c when assuming free-streaming of partons at $\tau < \tau_0$. However Luzum & Romatchke [49] argue that the large initial eccentricity of CGC geometry allows a bigger τ_0 (up to 1.5fm/c) for free-streaming, without destroying the agreement of their calculation with experimental data. Note that free-streaming is an extreme assumption, since partons always interact with each other and build up flow even if the matter is not in local thermal equilibrium [50]. This is especially true for jet energy loss which does not explicitly require local equilibrium. Nevertheless, it is an interesting question to ask whether the high p_T anisotropy due to jet quenching can provide any constraints on τ_0.

Current implementations of the pre-equilibrium energy loss are different among various pQCD models. The value of τ_0 typically varies in 0-0.6 fm/c. Some calculations assume $\hat{q} = 0$, while others assume it is constant at $\tau < \tau_0$ [4, 13, 51, 52]. Although both can describe the single inclusive suppression, the extracted $\hat{q}$ at τ_0 can differ by as much as a factor of two [53]. In this work, we tried three different formalisms to model the pre-equilibrium energy loss.

- Jet propagate freely to $\tau_0 = l_0/c$, then radiative energy loss and LPM interference are switched on.

$$\begin{aligned} I_a &= \int_{l_0}^{\infty} dl\ (l-l_0)\frac{\rho(\overrightarrow{\mathbf{r}}+l\widehat{\mathbf{v}})}{l} \\ &= \int_0^{\infty} dl\ \frac{l}{l+l_0}\rho(\overrightarrow{\mathbf{r}}+(l+l_0)\widehat{\mathbf{v}}) \end{aligned} \tag{9}$$

- LPM effects starts at $\tau = 0$, but its contribution to energy loss is truncated at $\tau < \tau_0$.

$$\begin{aligned} I_b &= \int_0^{\infty} dl\ \frac{\rho(\overrightarrow{\mathbf{r}}+l\widehat{\mathbf{v}})}{l} \times \begin{cases} 0 & l \le l_0 \\ l & l > l_0 \end{cases} \\ &= \int_{l_0}^{\infty} dl\ \rho(\overrightarrow{\mathbf{r}}+l\widehat{\mathbf{v}}) \end{aligned} \tag{10}$$

  This functional form is motivated by oftenly made claims similar to the one from Ref. [13]: *"For times prior to 0.6 fm/c, i.e. the starting point of the RFD simulation, we neglect any medium effects, i.e. assume $\hat{q} = 0$. Note that for a purely radiative energy loss model where the average energy loss grows quadratically with path length in a constant medium the effect of initial time dynamics is systematically suppressed and no strong dependence of the energy loss on variations of the initial time is observed."*

- Radiative energy loss is on all the time, but the experienced density is assumed to linearly increase with time and reach the local density at τ_0.

$$I_c = \int_0^{\infty} dl\ \times \begin{cases} \rho(\overrightarrow{\mathbf{r}}+l_0\widehat{\mathbf{v}})\frac{l}{l_0} & l \le l_0 \\ \rho(\overrightarrow{\mathbf{r}}+l\widehat{\mathbf{v}}) & l > l_0 \end{cases} \tag{11}$$

  This effectively implies a $\hat{q}$ that grows and reach maximum at τ_0.

Fig. 16 shows the calculation for various values of τ_0 from 0 to 2.0 fm/c for the three cases in the rotated frame. We find that the I_a exhibits the strongest dependence on τ_0. The calculated v_2 increases almost linearly with τ_0, and reaches the experimental data at $\tau_0 \sim$1.5 fm/c. This time is somewhat smaller than a similar analysis from Pantuev [54], who need $\tau_0 \sim 2-3$ fm/c to match the data. τ_0 is smaller in our case because we include eccentricity fluctuation. The increase of v_2 with τ_0 can be attributed to increasingly larger contribution from jets originated from the corona region of the overlap, whose size is proportional to τ_0 [54] [2]. Note that the dependence jet quenching v_2 on τ_0 is just the opposite of that for elliptic flow, the latter always decreases with increasing τ_0.

For second functional form, I_b, we find that the truncation of contribution at $\tau < \tau_0$ does simulate the suppression of the early contribution due to quadratic path length dependence. However, I_b exhibits a much weaker dependence on τ_0 than I_a, so the two are not equivalent. The increase of v_2 reaches about 20% for $\tau_0 = 0.6$ fm/c and grows continuously thereafter. It reaches the experimental value at $\tau_0 = 2.0$ fm/c instead of $\tau_0 = 1.5$ fm/c for I_a.

As a more realistic scenario that takes into account some contributions from $\tau < \tau_0$, I_c exhibit much weaker dependence on τ_0. The change in v_2 is less than 10% at $\tau_0 < 0.6$ fm/c; but it again increases quickly at large τ_0 (> 1 fm/c), where matter integral is dominated by the corona region which has a large asymmetry.

A slightly different exploration of effects of early time energy loss has been reported in Ref. [53]. It assumes either a constant $\hat{q}$ ($\hat{q} = \hat{q}(\tau_0)$) or a $\hat{q}$ that decreases rapidly to its value at τ_0 ($\hat{q} = \hat{q}(\tau_0)\left(\frac{\tau_0}{\tau}\right)^{3/4}$). Both cases implies more pre-equilibrium contribution than I_c, thus we expect they have even weaker dependence on τ_0 than I_c. Note that it is generally true that calculation which has a smaller τ_0 or takes into account the contribution at $\tau < \tau_0$ always have smaller v_2, because the early part of the matter integral tends to be more isotropic.

Our calculation does not take into account the transverse expansion. As pointed out earlier [55, 56], the dependence on τ_0 is further suppressed if the radial flow is included. This is because the medium moves outwards at speed of v_T. Jets that are generated behind the fluid cell need to move and catch up with it. Thus matter integral decrease more slowly with τ_0 than the 1+1D case; Effectively, the radial flow tends to shrink the black core region and reduce the dependence on τ_0.

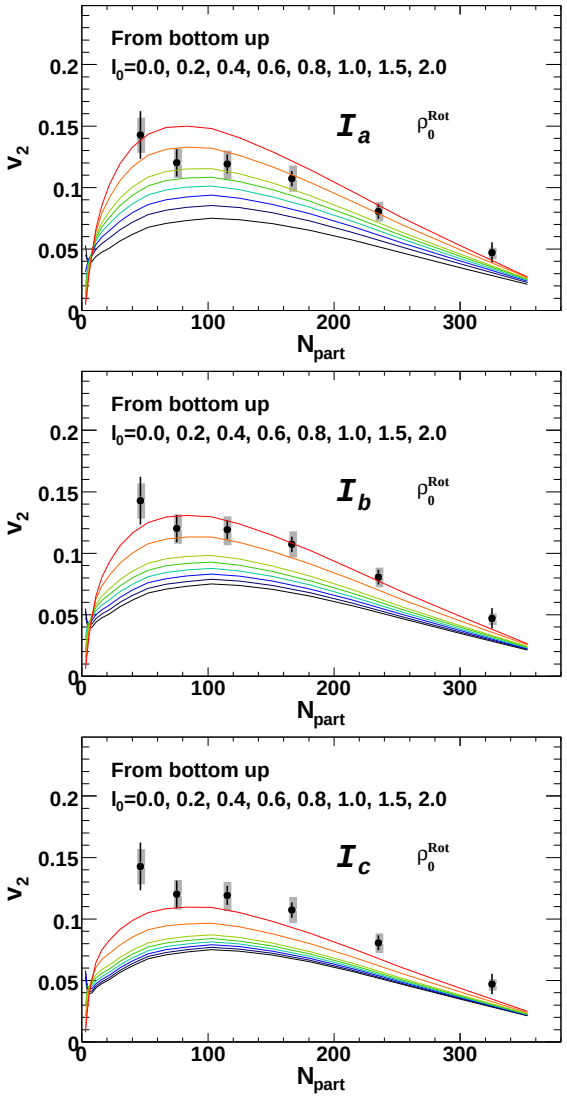

FIG. 16: (Color online) v_2 calculated using three different schemes for jet absorptions: I_a according to Eq. 9 (top panel), I_b according to Eq. 10 (middle panel), I_c according to Eq. 11 (bottom panel). In each cases, 8 different thermalization times range from l_0=0 to 2 fm are shown (curve is lower for smaller l_0).

F. How sensitive is $R_{\rm AA}$ to initial geometry and energy loss formula?

The setup of our model framework also provides a convenient way to study the centrality dependence of several other jet quenching observables, such as inclusive single hadron suppression $R_{\rm AA}$, inclusive away-side per-trigger

[2] This can be qualitatively understood as the following. Eq. 9 defines a corona region $l < l_0$ (I_a is less suppressed) and a core region $l > l_0$ (I_a is more suppressed), where l is the distance from the surface. The radial distribution of the initial positions for the surviving jets is largely defined by the requirement that $R_{AA} = 0.18$ or 18% jets survives in most central collisions. When l_0 is small, the corona volume is $< 18\%$, the surviving jets comes from both corona and core, and has a quite broad radial distribution. As l_0 or corona volume grows, more and more surviving jets originate from the corona region with larger anisotropy, the radial distribution narrows. Until corona volume reaches around 18%, most surviving jets comes from corona and the core become almost black.

yield suppression $I_{\rm AA}$ and its associated anisotropy $v_2^{I_{\rm AA}}$ (i.e. $I_{\rm AA}$ as function of angle with respect to the PP). It is rather straightforward for us to identify (similar to v_2) the most relevant control factors of the collision geometry and path length dependence for these observables. To preserve the flow of the main discussion, we focus this section on the inclusive $R_{\rm AA}$, since it coupled directly to the v_2 discussion. We refer the reader to some initial work on $I_{\rm AA}$ and $v_2^{I_{\rm AA}}$ in Appendix A.

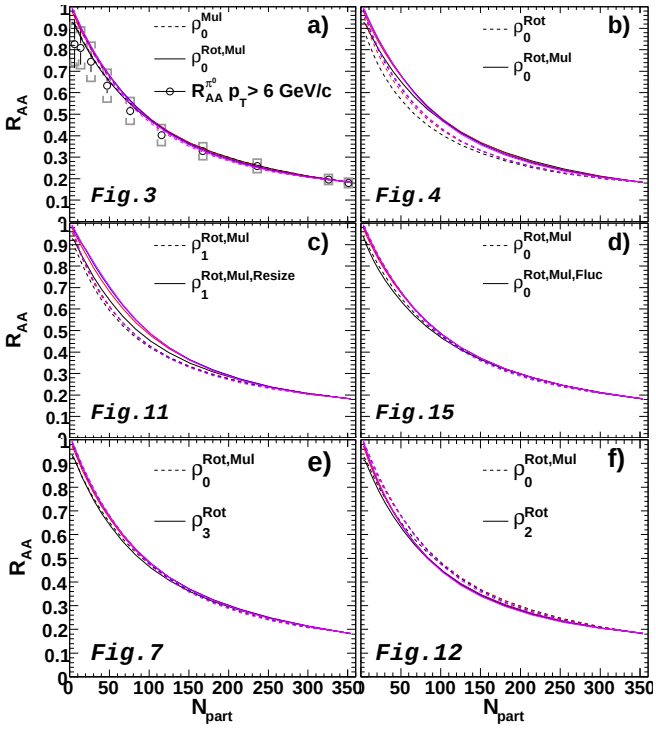

FIG. 17: (Color online) Each of the six panels show the comparison of centrality dependence of $R_{\rm AA}$ between two matter profiles (matter types are indicated) for $I_1 - I_4$ (8 curves in total). The corresponding v_2 figure for the same set of geometries is indicated in each panel. The first four panels shows the effects of switch on and off particular effect of the geometry, i.e. Rotation to participant plane for participant profile (panel a)), matching dN/dy for participant profile (panel b)), matching the size for collisional profile (panel c)), and including the additional fluctuation (panel d)). The remaining two panels show comparison between Glauber and CGC geometry (Panel e)) and between two Glauber geometries (Panel f)), respectively.

Fig. 17 shows the calculated $R_{\rm AA}$ in six different cases, with each one designed to check the sensitivity on one aspect of the geometry. From top to bottom and left to right, the lists of checked effects are:

a) Without ($\rho_0^{\rm Rot}$) and with ($\rho_0^{\rm Rot,Mul}$) eccentricity fluctuation. The corresponding v_2 comparisons are shown in Fig. 3.

b) Without ($\rho_0^{\rm Rot}$) and with ($\rho_0^{\rm Rot,Mul}$) matching the multiplicity. The corresponding v_2 comparisons are shown in Fig. 4.

c) Without ($\rho_1^{\rm Rot,Mul}$) and with ($\rho_0^{\rm Rot,Mul,Resize}$) readjusting the RMS size. The corresponding v_2 are indicated by the dashed and solid lines in Fig. 11.

d) Without ($\rho_1^{\rm Rot,Mul}$) and with ($\rho_1^{\rm Rot,Mul,Fluc}$) additional fluctuation beyond rotation of the PP. The corresponding v_2 comparisons are shown in Fig. 15.

e) Glauber geometry based on ($\rho_0^{\rm Rot,Mul}$) versus CGC geometry ($\rho_3^{\rm Rot}$). The corresponding v_2 comparisons are shown in Fig. 7.

f) Two glauber geometries: participant profile ($\rho_0^{\rm Rot,Mul}$) versus two component profile ($\rho_2^{\rm Rot}$). The corresponding v_2 comparisons are shown in Fig. 12.

In each case, all four path length dependence $I_1 - I_4$ are shown with and without the particular effect under investigation. Fig. 18 compares the different choices of the thermalization time τ_0 in a broad range using formulation I_a (left panel) and I_c (right panel); The corresponding v_2 comparisons has been shown in Fig. 16.

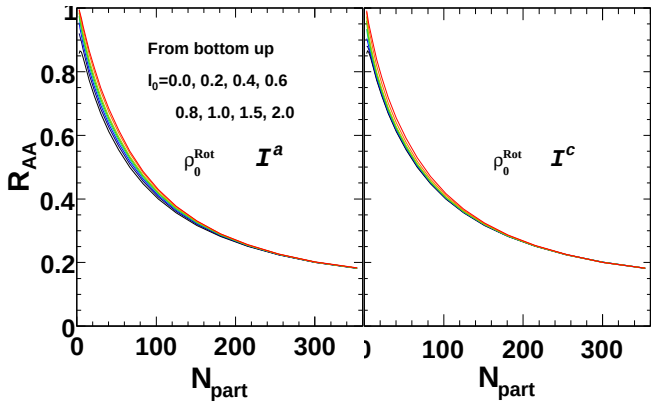

FIG. 18: (Color online) The centrality dependence of $R_{\rm AA}$ as function of thermalization time l_0/c; Two different jet absorption schemes are used, i.e. I_a in the left panel (Eq. 9) and I_c in the right panel (Eq. 11).

It appears that when jet absorption strength is tuned to reproduce the suppression in most central collisions, the centrality dependence of $R_{\rm AA}$ has limited sensitivity on different choices of the collision geometry and energy loss formula. This confirms previous observation [17, 48] that the centrality dependence of the $R_{\rm AA}$ has limited discriminating power to dynamics of the underlying energy loss mechanisms. This is partly due to the energy loss bias, but it is also related to the fact that $R_{\rm AA}$ has to vary monotonically between $R_{\rm AA} \sim 0.2$ at large $N_{\rm part}$ and $R_{\rm AA} \sim 1$ when $N_{\rm part} \to 0$. However, $R_{\rm AA}$ does exhibit some sensitivities for three cases, i.e. it increases somewhat for larger τ_0 (Fig. 18), stronger centrality dependence of dN/dy (Fig. 17b) and larger RMS size of the

matter profile (Fig. 17c) [3]. However the change is well within typical range of the experimental systematic errors. The situation is very different for v_2 or anisotropy of $R_{\rm AA}$, which is not a monotonic function of $N_{\rm part}$, and exhibit a much larger sensitivity to the variation of geometry and energy loss scheme.

IV. DISCUSSION AND SUMMARY

Table I summarize the sensitivity of v_2 and $R_{\rm AA}$ on the choices of matter profile and energy loss formula. The former includes fluctuation and shape distortion which affect the eccentricity, centrality dependence of multiplicity, and the size of the matter profile. The latter includes different choices of path length dependence and thermalization time. Overall, $R_{\rm AA}$ is not sensitive to these factors, while v_2 has fairly strong dependence on both initial geometry and energy loss formula. We can summarize the main findings for v_2 as the following.

- Eccentricity fluctuation has to be included in the jet quenching calculation, without it one can not account for the large v_2 observed in central collisions. We estimate that it leads to 15-20% increase of the v_2 in mid-centrality bin (Fig. 3).
- The residual event-by-event fluctuation, other than from eccentricity fluctuation, at most leads to 4-8% change in v_2 at $N_{\rm part} > 100$ (Fig. 15).
- A reasonable variation of the multiplicity dependence only significantly change the v_2 at $N_{\rm part} < 100$ (Fig. 4).
- CGC geometry always results in a larger v_2 than Glauber geometry at $N_{\rm part} > 150$. Depending on the choices of Glauber geometry, the increase ranges anywhere from 10% ($\rho_{\rm part}$, Fig. 7), 30% (two component profile ρ_2, Fig. 12), or 20%-> 50% ($\rho_{\rm coll}$, Fig. 11).
- v_2 is very sensitive to change of the RMS width σ_r of the profile, a 15% change in σ_r can lead to about 30-40% change in calculated v_2 (Fig. 11).

These same conclusions seem also apply for the anisotropy of away-side suppression $v_2^{I_{\rm AA}}$ (see Fig. 21), except that the sensitives seem to be much stronger. We stress that the dependence of jet quenching v_2 on geometry is different from that for the low p_T v_2 driven by collective expansion. The latter is sensitive only to the eccentricity of matter profile (item 1 and 3 in Table I).

Despite the rather complicated dependence on the initial geometry for jet quenching v_2, most of them, such as the fluctuation and distortion due to saturation, has been constrained qualitatively by elliptic flow data [29, 49]. Jet quenching v_2 appears to be rather sensitive to the choices of energy loss formula, thus making it an ideal observable to gain insights on energy loss mechanisms. Based on the comparison shown in Fig. 3 and 7, it seems that naive path length dependence motivated by radiative energy loss, I_1, is insufficient to describe the data for both Glauber and CGC geometry even with eccentricity fluctuations taken into account. It appears that either $2 < m < 3$ for Glauber geometry based on participant profile or $m \sim 2$ for CGC geometry, both with eccentricity fluctuations, have the best match with the data. Note that $m = 2$ corresponds to the AdS/CFT type of energy loss $\Delta E \propto l^3$ for a strongly coupled plasma [21]. Similar strong path length dependence is also observed for away-side suppression $I_{\rm AA}$ and it's anisotropous $v_2^{I_{\rm AA}}$ (see Fig. 20 and 21).

The jet quenching v_2 is also quite sensitive to thermalization time τ_0, but the sensitivity depends on the modeling of the pre-equilibrium energy loss. By assuming free-streaming up to $\tau_0 = 1.5$ fm/c and including eccentricity fluctuation, we can reproduce the experimental data with quadratic path length dependence of energy loss. However, inclusion of a very modest pre-equilibrium energy loss, e.g. I_c which assumes a $\hat{q}$ which linearly grow to $\hat{q}(\tau_0)$ at τ_0, already significantly suppressed the dependence on τ_0 up to 1 fm/c. We can draw similar conclusions for away-side suppression $I_{\rm AA}$ and the associated anisotropy $v_2^{I_{\rm AA}}$ (see Fig. 22 and 23).

The above discussion attested the value of jet quenching v_2 in understanding the roles of various geometry factors and to constrain the energy loss mechanisms. One can obtain more discriminating power by combining all jet quenching observables, v_2, $R_{\rm AA}$, $I_{\rm AA}$ and $v_2^{I_{\rm AA}}$ (see Appendix A for more discussions). Initial theoretical work already demonstrated the value of combining the $R_{\rm AA}$ and $I_{\rm AA}$ [8, 53], one can do a better job to also include calculation of v_2. It is worthy to point out that the study of high p_T v_2 benefited significantly from extensive experimental/theoretical work on the low p_T v_2, which has provided important constraints on the initial eccentricity. It would be interesting to see whether the reverse is true, i. e. whether jet quenching observables can provide useful new insights on the initial geometry to help the interpretation of the elliptic flow data.

In summary, using a simple jet absorption framework, we studied the sensitivity of jet quenching v_2 to various aspects of collision geometry and the path length dependence of energy loss. Besides the eccentricity, we found two other ingredients of the collision geometry, namely the centrality dependence of the matter integral and the relative size between the matter and jet profile, are important for jet quenching v_2. We compare the calculated

[3] Naively, one would expect the $R_{\rm AA}$ to decrease for larger σ_r since more jets originate from inside the profile. However this is only true if jet absorption strength κ remains the same. Since we always readjust κ such that $R_{\rm AA} \sim 0.18$ in most central bin, it almost cancels the expected suppression in large $N_{\rm part}$ and even make the peripheral bin less suppressed (Fig. 17c). This is very different from v_2, which always increase for larger σ_r (see Fig. 11).

TABLE I: The sensitivity of the v_2 and $R_{\rm AA}$ for various changes in matter profile (relative to participant profile) and energy loss schemes.

Types of changes	v_2	$R_{\rm AA}$
Fluctuation of RP angle	Increase by 15-30% for mid-centrality, much larger in central and peripheral (Fig. 3)	$< 5\%$
Additional fluctuation (relevant for e-b-e jet quenching calculation)	$\pm 5 - 10\%$ (Fig. 15)	$< 5\%$
Change in average shape	Increase by 15-30% for CGC (Fig. 7 and 8), by 10% for two component model (Fig. 12), 10-40% for $\rho_{\rm coll}$ profile (Fig. 11)	$< 5\%$
RMS size of matter profile (σ_r)	$\sim$0 to -10% change for CGC (compare Fig. 7 to 8), $\sim$10 to -40% change for $\rho_{\rm coll}$ (Fig. 11, compare dashed to solid line)	10% change for 10% difference
Centrality dependence of multiplicity	Important for $N_{\rm part} < 150$ (Fig. 4)	10-20% for mid-centrality
Power n for "l" dependence	Very sensitive	$< 5\%$
Thermalization time τ_0	Sensitive but depends on modeling of energy loss at $\tau < \tau_0$. For $\tau_0 = 0.6{\rm fm}/c$, it increases by $\sim 30\%$ for I_a, $< 15\%$ for I_b and $< 5\%$ for I_c. (see Fig. 16)	No, except for $N_{\rm part} < 100$

v_2 from both Glauber and CGC geometry with experimental data. A path length dependence stronger than the native $\Delta E \propto l^2$ dependence from radiative energy loss, as well as the inclusion of the eccentricity fluctuation are necessary in order to reproduce the v_2 data. A detailed comparison between Glauber and CGC geometry shows that a 15-30% increase of initial eccentricity in CGC only results in half the increase in calculated v_2 due to a small narrowing of the CGC geometry. This points to an interesting possibility: A large v_2 can be easily generated if the jet production profile is significantly narrower than the matter profile. This requires a transverse profile distribution that narrows with momentum or Bjorken variable $x = 2p_T/\sqrt{s}$. This happens for the nucleon-nucleon collisions [57, 58], however, we are not aware yet a physical mechanism to produce a significant narrowing at large x in heavy nuclei.

Our estimations are based on a simple jet absorption framework. Admittedly, it is too simplistic to give direct insight on the dynamics of the energy loss process. However it proves to be a useful tool for understanding the centrality dependence of various jet quenching observables, for identifying the most relevant factors in the collision geometry and path length dependence, as well as for estimating the sign and magnitude of the change as we vary those factors. We have documented all the matter and jet profile used in this study in [59]. They can be used as input for future more realistic jet quenching calculations.

Acknowledgement

We thank for valuable discussions; We thank H. J. Drescher, A. Dumitru and Y. Nara for providing the MC-KLN code. This research is supported by NSF under award number PHY-0701487.

APPENDIX A: $I_{\rm AA}$ AND ITS AZIMUTHAL ANISOTROPY?

Initial geometry should also leave footprints on the azimuthal distribution of the away-side jets. The appropriate observable for this purpose is the anisotropy of the per-trigger yield for the away-side jets, $I_{\rm AA}(\phi_{\rm trig} - \Psi_{\rm part})$, which reflects the path length dependence of the energy loss for the away-side jet. Due to the surface bias of the trigger jets, the away-side jets on average have longer path length to traverse, thus they are expected to exhibit stronger suppression and larger anisotropy. In this work, we calculate the anisotropy coefficient as

$$v_2^{I_{\rm AA}} = \langle I_{\rm AA} \cos 2(\phi_{\rm trig} - \Psi_{\rm part}) \rangle \tag{A1}$$

As a warm up exercise, Fig. 19 shows the azimuthal dependence of per-trigger yield suppression $I_{\rm AA}$ in 0-20% and 20-60% centrality, calculated for $\rho_0^{\rm Rot,Mul}$ profile, i.e. participant density profile in rotated frame and re-scaled

to match the dN/dy data. As one increase the power m of the path length dependence in I_m, $I_{\rm AA}$ for 20-60% bin shows a dramatic decrease in the out-of-plane direction where the path length is large, but only a modest decrease in the in-plane direction where the path length is small. That is because the suppression for a given centrality is largely determined by the typical matter integral $I_m \sim \langle L\rangle^m / \langle L_0^m\rangle^m$, which changes more rapidly for larger m. Here L_0^m is some typically length scale fixed in central collisions for m. Clearly, the increased sensitivity of large m can generate a large anisotropy, hence large $v_2^{I_{\rm AA}}$. However, the price one has to pay is that it leads to a large suppression in the 0-20% bin as shown in the left panel of Fig. 19. This is because a large $v_2^{I_{\rm AA}}$ naturally implies a strong suppression in central collisions, as long as the suppression is a monotonic function of the path length.

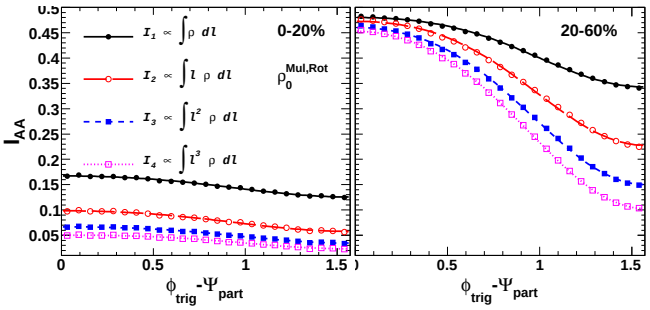

FIG. 19: (Color online) The $I_{\rm AA}(\phi_{\rm trig}-\Psi_{\rm part})$ for 0-20% (left panel) and 20-60% (right panel) centrality bins. The points are results of calculation, the line is a fit to $1+2v_2^{I_{\rm AA}}\cos 2\Delta\phi+2v_4^{I_{\rm AA}}\cos 2\Delta\phi$. We see a finite $v_4^{I_{\rm AA}}$ signal, but it is less than 10% of $v_2^{I_{\rm AA}}$, and is ignored in this study.

The jet absorption framework used in this work is a pure geometrical model, in that the calculated suppression depends only on the path length, thus it always predicts $I_{\rm AA} < R_{\rm AA}$ due to the longer path length of the away-side jet. However, experimental data seem to suggest that $I_{\rm AA} \gtrsim R_{\rm AA}$ [7, 60, 61]. This is because that the away-side associated hadron spectra is much flatter than the inclusive distribution, due to the requirement of a high p_T trigger. For a typical trigger of 5 GeV/c, the away-side conditional spectra in $p+p$ collisions at $\sqrt{s}=200$ GeV, if parameterized via a power law function $1/p_T^n$, has a power of $n=8$ in contrast to $n=4$ for inclusive hadrons [62]. A simple estimation shows that in order to reach the same level of suppression, it takes about 50% more energy loss for away-side jets than for inclusive jets [62]. What this means is that treating energy loss as absorption is not sufficient, a energy shift term is required as well. However phenomenologically, we can still use the jet absorption framework, if we allow the κ to also depend on power n, i.e a smaller κ is required for away-side jet due to a flatter input spectra. Such dependence in principle can be fixed by the $I_{\rm AA}$ data from STAR and PHENIX [7, 60, 61]. But we shall defer this improvement to a future study.

Nevertheless, current setup is sufficient for studying the sensitivity of $I_{\rm AA}(\Delta\phi)$ on the choices of underlying collision geometry. Fig. 20 and Fig. 21 summarize the relative change of the inclusive $I_{\rm AA}$ and its anisotropy $v_2^{I_{\rm AA}}$, respectively, as one vary various aspects of the collision geometry. The six cases in both figures corresponds to the same change in collision geometry as in Fig. 17 for inclusive $R_{\rm AA}$, i.e. **a)** eccentricity fluctuation, **b)** matching the multiplicity, **c)** re-scale the geometrical size σ_r, **d)** additional fluctuation not included by rotation, **f)** Default Glauber geometry versus CGC geometry, **g)** Default Glauber geometry versus two component geometry.

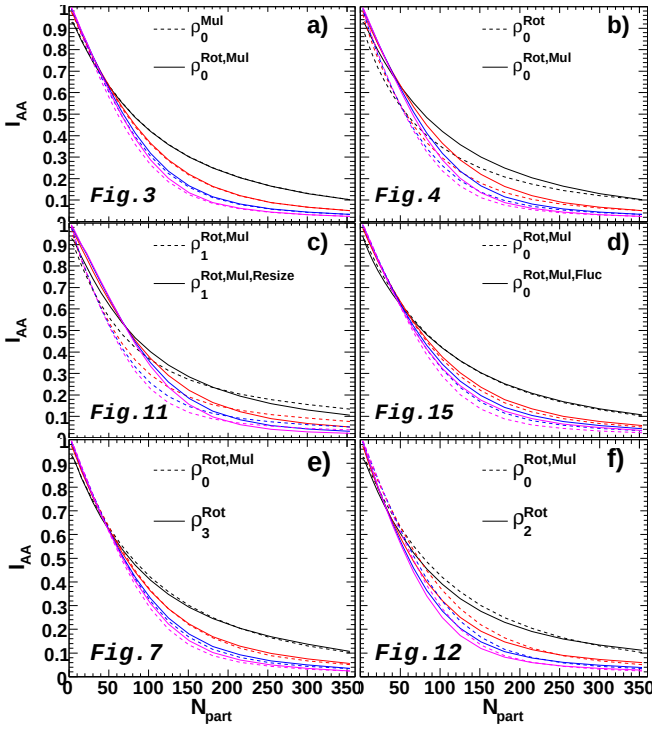

FIG. 20: (Color online) Conventions are similar to Fig. 17. Each of the six panels show the comparison of centrality dependence of $I_{\rm AA}$ between two matter profiles (matter types are indicated) for I_1-I_4 (8 curves in total); the corresponding v_2 figures for the same set of geometries are indicated in each panel. The first four panels shows the effects of switch on and off particular effect of the geometry, i.e. rotation of participant plane for participant profile (panel a)), matching dN/dy for participant profile (panel b)), matching the size for collisional profile (panel c)), and including the additional fluctuation (panel d)). The remaining two panels show comparison for Default Glauber vs. CGC geometry (Panel e)) and between two Glauber geometries (Panel f)), respectively.

In general, we see that $I_{\rm AA}$ and $v_2^{I_{\rm AA}}$ are much more sensitive to their counterpart single particle observables, $R_{\rm AA}$ and v_2. They are also very sensitive to both the path length dependence and thermalization time τ_0 (see Fig. 22 and Fig. 23). In one case (Fig. 21c)), the $v_2^{I_{\rm AA}}$ even becomes negative in central collisions, reflecting the

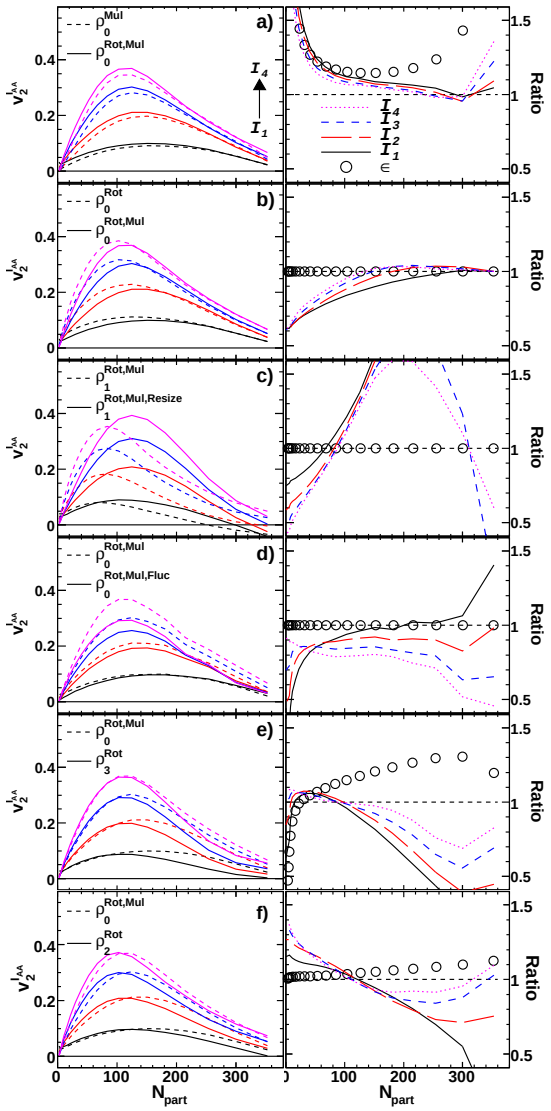

FIG. 21: (Color online) Conventions are similar to Fig. 17. Each of the six rows show: (left panel) the comparison of centrality dependence of $v_2^{I_{\rm AA}}$ between two matter profiles (matter types are indicated), (right panel) The corresponding ratios together with ratios of eccentricities. The corresponding $v_2^{I_{\rm AA}}$ plot for the same set of geometries are indicated in each panel. The first four rows show the effects of switch on and off particular effect of the geometry, i.e. Rotation to participant plane for participant profile (Row a)), matching dN/dy for participant profile (Row b)), matching the size for collisional profile (Row c)), and including the additional fluctuation (Row d)). The remaining two rows show comparison for Default Glauber vs. CGC geometry (Row e)) and between two Glauber geometries (Row f)), respectively.

dominance of tangential emission when collision profile is used as matter profile (ρ_1). This is the case because ρ_1 has the narrowest profile (15% smaller than participant profile), such that more jets are generated on the surface and can survive if emitted tangentially. Unlike the v_2, the change in $v_2^{I_{\rm AA}}$, when tuned to same multiplicity and

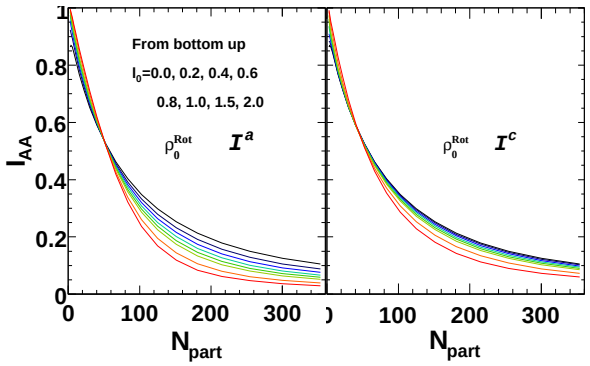

FIG. 22: (Color online) The centrality dependence of $I_{\rm AA}$ as function of thermalization time l_0; Two different jet absorption schemes are used, i.e. I_a in the left panel (Eq. 9) and I_c in the right panel (Eq. 11).

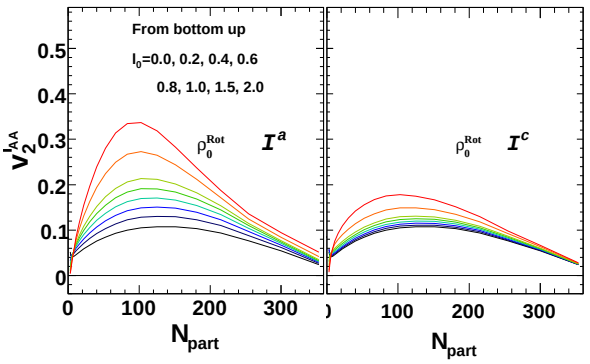

FIG. 23: Similar to Fig. 22, except plotted for $v_2^{I_{\rm AA}}$.

average, is not proportional to the corresponding change in ϵ. The only change that $I_{\rm AA}$ and $v_2^{I_{\rm AA}}$ is not sensitive to is the fluctuation of the PP angle.

APPENDIX B: COMMENTS ON FINITE NUCLEON SIZE EFFECT, EVENT-BY-EVENT FLUCTUATION ETC

We can show explicitly why the finite nucleon size is not important for v_2 calculation except in most peripheral collisions. We notice that the finite nucleon size leads to an increase of the variance matter profile, but does not change the orientation of the rotated frame:

$$\begin{aligned}
\sigma_x'^2 &\rightarrow \sigma_x'^2 + r_0^2 \\
\sigma_y'^2 &\rightarrow \sigma_y'^2 + r_0^2 \\
\sigma_{xy}' = 0 &\rightarrow \sigma_{xy}' = 0 \\
\sigma_r'^2 &\rightarrow \sigma_r'^2 + r_0^2 \\
\epsilon^{\rm part} &\rightarrow \epsilon^{\rm part}\left(1 + \frac{r_0^2}{\sigma_r^2}\right)
\end{aligned}$$

The eccentricity decreases a little bit due to smearing of n-n overlap function. However, for a typical fireball size of $\sigma_r = 3$fm, this is only 1.7% change in the eccentricity [4]. The RMS size of the ellipsoid also increases by a few %, but the corresponding jet production profile increases by the same amount, resulting almost no change on the calculated v_2. Fig. 24 shows the ratio of the v_2 for event averaged ρ_0 calculated assuming the nucleon profile follows either the δ function or a Gauss function with width $r_0 = 0.4$ fm. The differences of v_2 are well within 3%, except at $N_{\rm part} < 20$ where $r_0 = 0.4$ fm case is smaller.

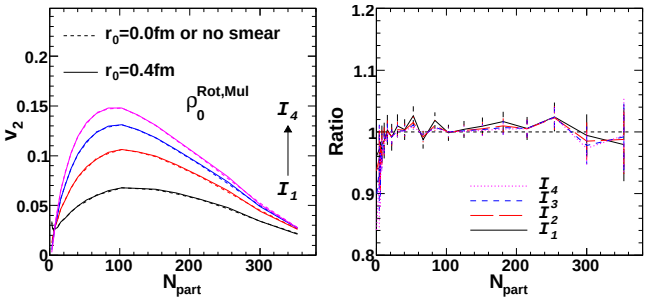

FIG. 24: (Color online) comparison of the v_2 for Glauber geometry, which are filled either according to center positions of nucleons or assuming Gauss profiles with a width of 0.4 fm.

Note that similar also appears in MC-KLN, which assumes participating nucleon are disks of finite size in filling the participant profile distribution (in addition to assuming finite nucleon size for determining whether it is a participant). This is illustrated by Fig. 25, which compares the v_2 results for the same Glauber geometry determined with either PHOBOS code or MC-KLN code. The ratio drops at $N_{\rm part} < 20$ similar to Fig. 24. As a side note, we point out that this plot also confirmed the consistency between the PHOBOS code or MC-KLN code for calculating the Glauber geometry when running with the same parameters.

We have seen that the event-by-event fluctuation leads to large dispersion of the distribution of various geometrical variables, such as eccentricity and RMS size in Fig. 13. Yet, the mean values seem to be insensitive to whether they are calculated for each event then averaged over many event or they are calculated directly from the averaged profile. As an example, Fig. 26 compares the eccentricity averaged over values calculated event by event $\left\langle \frac{\sigma_y'^2-\sigma_x'^2}{\sigma_y'^2+\sigma_x'^2} \right\rangle$ with the eccentricity calculated from the average profile $\frac{\langle\sigma_y'^2\rangle-\langle\sigma_x'^2\rangle}{\langle\sigma_y'^2\rangle+\langle\sigma_x'^2\rangle}$. The ratios are shown in the right panel for both $\epsilon_{\rm RP}$ and $\epsilon_{\rm part}$. As one can see, the difference is $< 2\%$ for $\epsilon_{\rm part}$, and somewhat larger for $\epsilon_{\rm RP}$ [5]. This is quite remarkable, given the sharp visual contrast between the lumpiness of event-by-event profile and smoothness of the average profile (see Fig. 27).

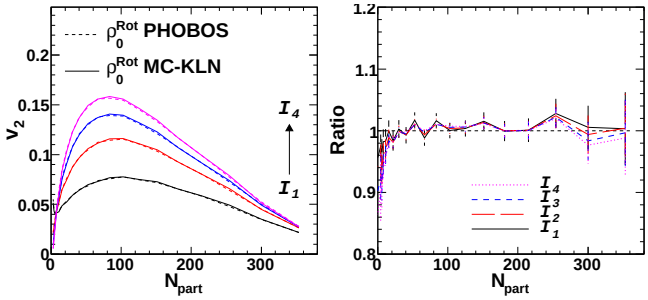

FIG. 25: (Color online) comparison of the v_2 for Glauber geometry calculated using PHOBOS code and MC-KLN code.

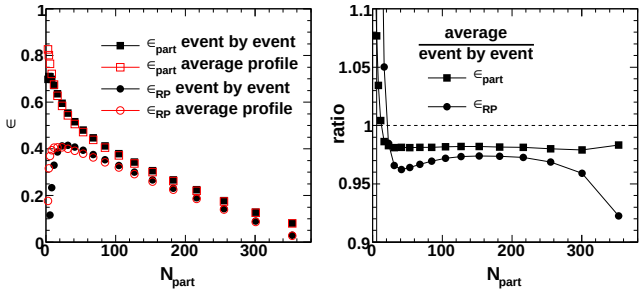

FIG. 26: (Color online) Left panel: the standard (circles) and participant (boxes) eccentricity either by averaging over their event-by-event value (filled symbols) or calculated directly from the averaged matter profiles (open symbols). Right panel: the corresponding ratios for the standard and participant eccentricity.

Nevertheless, the good news is that the average profile seems to preserve most of the relevant geometrical information. For example, one can calculate the eccentricity directly from the overall matter profile instead of calculating it event by event then averaged over many events.

[4] The impact is somewhat larger for $\epsilon_{\rm RP}$, i.e. average without rotation

[5] The agreement generally worsens when the width of the distribution become large relative to the mean value, which is the case for $\epsilon_{\rm RP}$.

[1] K. Adcox *et al.*, Nucl. Phys. A **757** (2005) 184; J. Adams *et al.*, Nucl. Phys. A **757** (2005) 102; B. B. Back *et al.*, Nucl. Phys. A **757** (2005) 28; I. Arsene *et al.*, Nucl. Phys. A **757** (2005) 1.

[2] M. Gyulassy, I. Vitev, X. N. Wang and B. W. Zhang, arXiv:nucl-th/0302077.

[3] U. A. Wiedemann, arXiv:0908.2306 [hep-ph].

[4] A. Majumder and M. Van Leeuwen, arXiv:1002.2206 [hep-ph].

[5] K. Adcox *et al.*, Phys. Rev. Lett. **88**, 022301 (2002)

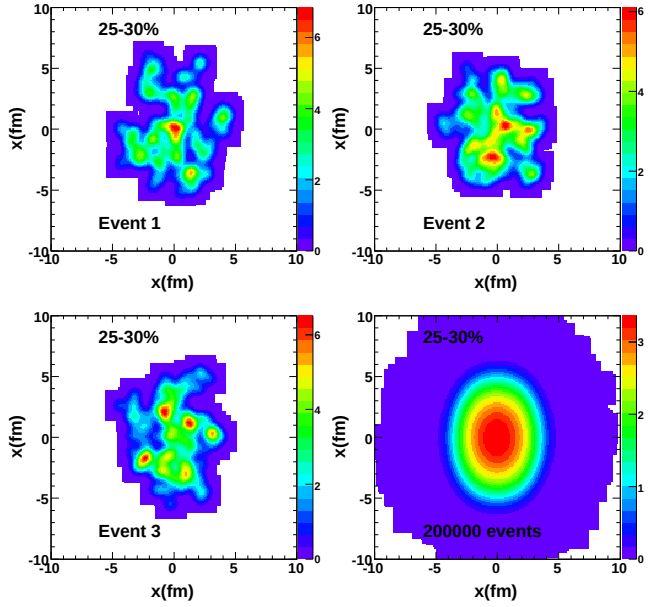

FIG. 27: (Color online) The event-by-event participant profiles ($\rho_0^{\rm Rot}$) for 3 typical events and profile averaged over 200k events for 25-30% centrality selection. Nucleons are assumed to have a Gauss profile with a width of $r_0 = 0.4$ fm; All events have been shifted to center of gravity and rotated to participant plane.

[6] I. Vitev and M. Gyulassy, Phys. Rev. Lett. **89**, 252301 (2002)
[7] A. Adare *et al.*, Phys. Rev. C **78**, 014901 (2008)
[8] H. Zhang, J. F. Owens, E. Wang and X. N. Wang, Phys. Rev. Lett. **98**, 212301 (2007)
[9] A. Adare *et al.*, Phys. Rev. C **80**, 024908 (2009)
[10] B. I. Abelev *et al.* arXiv:0912.1871 [nucl-ex].
[11] H. Zhang, J. F. Owens, E. Wang and X. N. Wang, Phys. Rev. Lett. **103**, 032302 (2009)
[12] G. Y. Qin, J. Ruppert, C. Gale, S. Jeon and G. D. Moore, Phys. Rev. C **80**, 054909 (2009)
[13] S. A. Bass *et al.* Phys. Rev. C **79**, 024901 (2009)
[14] B. Muller, Prog. Theor. Phys. Suppl. **174**, 103 (2008).
[15] S. Peigne and A. V. Smilga, Phys. Usp. **52**, 659 (2009) [Usp. Fiz. Nauk **179**, 697 (2009)]
[16] E. V. Shuryak, Phys. Rev. C **66**, 027902 (2002)
[17] A. Drees, H. Feng and J. Jia, Phys. Rev. C **71**, 034909 (2005)
[18] R. Wei Nucl. Phys. A **830**, 175C (2009)
[19] A. Adare *et al.* Phys. Rev. Lett. **98**, 172301 (2007)
[20] S. Wicks, W. Horowitz, M. Djordjevic and M. Gyulassy, Nucl. Phys. A **784**, 426 (2007)
[21] S. S. Gubser, D. R. Gulotta, S. S. Pufu and F. D. Rocha, JHEP **0810**, 052 (2008)
[22] H. Liu, K. Rajagopal and U. A. Wiedemann, Phys. Rev. Lett. **97**, 182301 (2006)
[23] C. Marquet and T. Renk, Phys. Lett. B **685**, 270 (2010)
[24] J. Liao and E. Shuryak, Phys. Rev. Lett. **102**, 202302 (2009)
[25] M. L. Miller, K. Reygers, S. J. Sanders and P. Steinberg, Ann. Rev. Nucl. Part. Sci. **57**, 205 (2007)
[26] H. J. Drescher, A. Dumitru, A. Hayashigaki and Y. Nara, Phys. Rev. C **74**, 044905 (2006)
[27] B. Alver *et al.*, Phys. Rev. C **77**, 014906 (2008)
[28] H. J. Drescher and Y. Nara, Phys. Rev. C **75**, 034905 (2007)
[29] T. Hirano and Y. Nara, Phys. Rev. C **79**, 064904 (2009)
[30] W. Broniowski, P. Bozek and M. Rybczynski, Phys. Rev. C **76**, 054905 (2007)
[31] B. Alver, M. Baker, C. Loizides and P. Steinberg, arXiv:0805.4411 [nucl-ex].
[32] D. Kharzeev, E. Levin and M. Nardi, Nucl. Phys. A **730**, 448 (2004) [Erratum-ibid. A **743**, 329 (2004)]
[33] D. Kharzeev and M. Nardi, Phys. Lett. B **507**, 121 (2001)
[34] B. B. Back *et al.* Phys. Rev. C **65**, 061901 (2002)
[35] P. F. Kolb and U. W. Heinz, arXiv:nucl-th/0305084.
[36] A. K. Chaudhuri, arXiv:0801.3180 [nucl-th].
[37] A. Adare *et al.*, Phys. Rev. Lett. **101**, 232301 (2008)
[38] D. A. Teaney, arXiv:0905.2433 [nucl-th].
[39] S. S. Adler *et al.* Phys. Rev. C **71**, 034908 (2005) [Erratum-ibid. C **71**, 049901 (2005)]
[40] B. Alver *et al.* Phys. Rev. C **80**, 011901 (2009)
[41] I. Vitev, Phys. Lett. B **639**, 38 (2006)
[42] A. Dainese, C. Loizides and G. Paic, Eur. Phys. J. C **38**, 461 (2005)
[43] T. Renk, J. Ruppert, C. Nonaka and S. A. Bass, Phys. Rev. C **75**, 031902 (2007)
[44] C. Nonaka and S. A. Bass, Phys. Rev. C **75**, 014902 (2007)
[45] J. L. Nagle, P. Steinberg and W. A. Zajc, Phys. Rev. C **81**, 024901 (2010)
[46] A. B. Migdal, Phys. Rev. **103**, 1811 (1956).
[47] P. F. Kolb, J. Sollfrank and U. W. Heinz, Phys. Rev. C **62**, 054909 (2000)
[48] K. J. Eskola, H. Honkanen, C. A. Salgado and U. A. Wiedemann, Nucl. Phys. A **747**, 511 (2005)
[49] M. Luzum and P. Romatschke, Phys. Rev. C **78**, 034915 (2008) [Erratum-ibid. C **79**, 039903 (2009)]
[50] J. Vredevoogd and S. Pratt, Phys. Rev. C **79**, 044915 (2009)
[51] B. Schenke, C. Gale and S. Jeon, Phys. Rev. C **80**, 054913 (2009)
[52] A. Majumder, C. Nonaka and S. A. Bass, Phys. Rev. C **76**, 041902 (2007)
[53] N. Armesto, M. Cacciari, T. Hirano, J. L. Nagle and C. A. Salgado, J. Phys. G **37**, 025104 (2010)
[54] V. S. Pantuev, JETP Lett. **85**, 104 (2007)
[55] I. P. Lokhtin, A. M. Snigirev and I. Vitev, arXiv:hep-ph/0212061.
[56] T. Renk and K. Eskola, Phys. Rev. C **75**, 054910 (2007)
[57] L. Frankfurt, M. Strikman and C. Weiss, Phys. Rev. D **69**, 114010 (2004)
[58] X. D. Ji, Phys. Rev. Lett. **91**, 062001 (2003)
[59] We have placed the 2D profile functions in 5% centrality bin for participant density, collision density and gluon density with eccentricity fluctuation at https://www.phenix.bnl.gov/WWW/publish/jjia/glauber/profile/profile.html. They can be used as input for viscous hydrodynamics and realistic jet quenching model calculations.
[60] A. Adare *et al.*, arXiv:1002.1077 [nucl-ex].
[61] J. Adams *et al.*, Phys. Rev. Lett. **97**, 162301 (2006)
[62] J. Jia, Int. J. Mod. Phys. E **16**, 2000 (2007)